U.S. Department
of Transportation
National Highway
Traffic Safety
Administration

NHTSA

DOT HS 813 817

August 2026

Comparative Analysis of Impedance and Gas Sensor Diagnostics for LFP/Graphite Cell Failures

This page is intentionally left blank.

DISCLAIMER

This publication is distributed by the U.S. Department of Transportation, National Highway Traffic Safety Administration, in the interest of information exchange. The opinions, findings, and conclusions expressed in this publication are those of the authors and not necessarily those of the Department of Transportation or the National Highway Traffic Safety Administration. The United States Government assumes no liability for its contents or use thereof. If trade or manufacturers' names or products are mentioned, it is because they are considered essential to the object of the publication and should not be construed as endorsement. The United States Government does not endorse products or manufacturers.

NOTE: This report is published in the interest of advancing motor vehicle safety research. While the report may provide results from research or tests using specifically identified motor vehicle models, it is not intended to make conclusions about the safety performance or safety compliance of those motor vehicles, and no such conclusions should be drawn.

Suggested APA Format Citation:

Torres-Castro, L., Bates, A. M., Quintana, G., & Gray, L. (2026, August). *Comparative analysis of impedance and gas sensor diagnostics for LFP/graphite cell failures* (Report No. DOT HS 813 817). National Highway Traffic Safety Administration. https://doi.org/10.21949/2ebz-fw17

This page is intentionally left blank.

Technical Report Documentation Page

1. Report No.	2. Government Accession No.	3. Recipient's Catalog No.
DOT HS 813 817		

4. Title and Subtitle	5. Report Date
Comparative Analysis of Impedance and Gas Sensor Diagnostics for LFP/Graphite Cell Failures	August 2026
	6. Performing Organization Code
7. Authors	8. Performing Organization Report No.
Loraine Torres-Castro, Alex M. Bates, Genaro Quintana, Lucas Gray	
9. Performing Organization Name and Address	10. Work Unit No. (TRAIS)
Sandia National Laboratories 1515 Eubank Blvd Se Albuquerque, NM 87123	11. Contract or Grant No. IAA
12. Sponsoring Agency Name and Address	13. Type of Report and Period Covered
National Highway Traffic Safety Administration 1200 New Jersey Avenue SE Washington, DC 20590	Final Report, November 2027 – September 2025
	14. Sponsoring Agency Code

15. Supplementary Notes

Digital Object Identifier: https://doi.org/10.21949/2ebz-fw17

16. Abstract

Lithium-ion battery cells subjected to abuse rapidly enter "thermal runaway," characterized by an uncontrolled rise in temperature. This poses significant risks, potentially leading to catastrophic failures such as off-gassing, fires, and explosions. This report assesses early detection methods for cell failure in lithium-ion batteries used in electric vehicles. The performance of rapid electrochemical impedance spectroscopy and commercially available gas sensors, including volatile organic compounds, and hydrogen sensors, were assessed under overtemperature and overcharge conditions using lithium iron phosphate graphite-based pouch cells. Experiments were conducted on single cells and three configurations: one series, four parallel (1s4p) four series, one parallel (4s1p); and two series, four parallel (4p2s) packs. Under overtemperature conditions, impedance spectroscopy consistently identified internal degradation prior to failure, providing the longest warning times. During overcharge, gas sensors were more responsive, particularly in larger packs where venting occurred rapidly and before measurable impedance changes. Pack architecture influenced both the severity of failure and the sensitivity of diagnostic signals. These results suggest that no single technique provides complete coverage across abuse scenarios, supporting the need for integrated diagnostics that account for system complexity in modern lithium-ion batteries.

17. Key Words	18. Distribution Statement
early detection, battery safety, thermal runaway, diagnostics, lithium-ion	Document is available to the public from the DOT, BTS, National Transportation Library, Repository & Open Science Access Portal, https://rosap.ntl.bts.gov.

19. Security Classif. (of this report)	20. Security Classif. (of this page)	21. No. of Pages	22. Price
Unclassified	Unclassified	50	

Form DOT F 1700.7 (8-72) Reproduction of completed page authorized

This page is intentionally left blank.

Table of Contents

List of Figures

List of Tables

List of Acronyms and Abbreviations

1s4p	one series, four parallel pack
4p2s	four parallel, two series pack
4s1p	four series, one parallel pack
cell-HR	cell heating rate
CO_2	carbon dioxide
DAQ	data acquisition
DEC	diethyl carbonate
DMC	dimethyl carbonate
EIS	electrochemical impedance spectroscopy
EMC	ethyl methyl carbonate
FTIR	Fourier-transform infrared spectroscopy
Gr	graphite
H_2	hydrogen
HR	heating rate
LCO	lithium cobalt oxide
LFP	lithium iron phosphate
NMC	lithium nickel manganese cobalt oxide
OC	overcharge
OT	overtemperature
PID	proportional-integral-derivative
SEI	solid electrolyte interphase
SOC	state-of-charge
TC	thermocouple
VOC	volatile organic compound

Executive Summary

Lithium-ion battery cells subjected to abuse can rapidly enter "thermal runaway," a state characterized by uncontrolled rise in temperature. It poses significant risks, potentially leading to catastrophic failures such as off-gassing, fires, and explosions. As lithium-ion batteries increase in capacity and scale, the need for early detection of cell failure becomes more critical to ensuring safety. This study evaluates the diagnostic response of two techniques, rapid electrochemical impedance spectroscopy and commercially available gas sensors that detect when lithium iron phosphate, graphite-based cells are subjected to overtemperature and overcharge. Testing was conducted across four configurations:

- single cells;
- a one series, four parallel (1s4p) pack;
- a four series, one parallel (4s1p) pack used only in overcharge testing; and
- and a four parallel, two series (4p2s) pack used only in overtemperature testing.

These were chosen to assess how system complexity and architecture influence diagnostic behavior.

Under thermal abuse conditions that we refer to here as overtemperature, impedance spectroscopy consistently enabled earlier detection of cell degradation in the single-cell and 1s4p configurations. In these cases, changes in resistance linked to internal damage were observed well before cell venting or failure onset. Although gas sensors responded reliably, they typically activated after electrochemical changes were evident. The slower heat propagation in the 1s4p pack allowed impedance features to remain measurable and distinct, offering lead time for potential intervention. In the 4p2s pack, gas sensors triggered earlier, suggesting that system complexity can reduce the sensitivity or timing of electrochemical diagnostics.

During overcharge testing, diagnostic behavior shifted. Gas sensors became more responsive, particularly in the 1s4p and 4s1p packs, where reactions progressed rapidly once the cell exceeded their charge limits. In these cases, venting and gas generation often preceded detectable impedance changes, compressing the window between failure initiation and electrochemical response. Some sensors such as VOC1 (Li-ion Tamer),[1] showed delayed or inconsistent activation, raising concerns about long-term reliability, calibration drift, and potential challenges with sensor placement in field applications.

This study shows that neither impedance measurements nor gas sensors alone provide complete early detection across all abuse modes. While impedance techniques offer clear benefits during overtemperature events, their effectiveness diminishes in overcharge conditions, particularly in larger or electrically complex systems. Gas sensors, though effective during overcharge, are limited by their reliance on venting and variable response times. Reliable early detection will depend on integrated approaches that combine electrochemical, thermal, and gas-phase diagnostics. These strategies must account for cell-to-cell variation, pack architecture, and system-level signal interference. Emphasis should be given to sensor placement, real-time signal interpretation, and redundancy in larger high-voltage systems, where local failure signals may be masked by noise or system complexity.

[1] Honeywell International Inc., Charlotte, NC.

This page is intentionally left blank.

Introduction

The widespread deployment of lithium-ion batteries across sectors such as electric vehicles, grid energy storage, aerospace, and consumer electronics has intensified the need for robust safety strategies. Although these systems offer high energy density and long cycle life, their performance and stability under abusive conditions, including overtemperature and overcharge, remain critical concerns. Detection and response to emerging faults is essential in preventing a thermal runaway state that leads to venting, fire, or explosion. As battery systems increase in size and energy, early detection of instability becomes a prerequisite for safe operation.

Conventional battery management systems typically rely on basic voltage, current, and surface temperature monitoring. However, these parameters often provide insufficient early warning. Thermal runaway can progress rapidly once initiated, leaving little time for mitigation. In response, standardized safety requirements emphasize the need for advanced diagnostics capable of issuing a warning at least 5 minutes before the onset of a dangerous event. Achieving this level of foresight demands techniques that can identify subtle, internal indicators of degradation before external symptoms become evident.

Recent studies have explored in-operando diagnostic methods designed to detect early signs of instability. Among these, electrochemical impedance spectroscopy and off-gas sensing have emerged as two of the most promising approaches. EIS measures a cell's impedance over a range of frequencies, revealing changes in internal electrochemical processes such as solid-electrolyte interphase breakdown, lithium plating, or localized heat generation. Rapid EIS techniques, including multi-sine and odd-random phase variants, have demonstrated the ability to detect precursors to failure several minutes before venting, particularly in cells with lithium iron phosphate cathodes and graphite anodes (Klink et al., 2021; Torres-Castro et al., 2024). However, implementing EIS across large-format battery packs introduces challenges related to signal resolution, per-cell access, and system integration.

Off-gas sensing offers a complementary diagnostic path, targeting carbon dioxide, hydrogen, and volatile organic compounds that are emitted during early-stage electrolyte and electrode degradation (Finegan et al., 2015; Gachot et al., 2012; Sloop et al., 2003). These gases often appear before visible damage or fire, offering a viable early warning signal. Research has shown that off-gas sensors can detect concentrations of CO_2 and H_2 well before thermal runaway, and their ability to monitor a shared environment makes them attractive for pack-level diagnostics (Cai et al., 2019, 2021; Hill et al., 2013; Zhang et al., 2024). Nevertheless, their effectiveness is influenced by gas dispersion dynamics, sensor placement, and the specific cell chemistry involved.

In addition to EIS and gas sensing, several other techniques have been investigated. These include acoustic emission monitoring, strain and pressure sensing, embedded thermal probes, and data-driven methods using machine learning. Such approaches can identify early physical or statistical anomalies, adding further layers of safety. For example, acoustic methods have detected subtle structural changes such as separator deformation or gas accumulation, while current-sharing imbalances between parallel cells have been used to flag emerging faults (Appleberry et al., 2022).

Abuse scenarios generally fall into two broad categories: thermal, such as OT, and electrical, such as OC or internal short circuit. The effectiveness of a given diagnostic method depends strongly on the nature of the abuse. EIS typically performs best during thermal abuse, detecting

impedance changes as internal temperatures begin to rise. Gas sensors are often more responsive in OC scenarios, where electrochemical reactions produce volatile species before significant heat buildup occurs. Reliable early fault detection requires a holistic approach that extends beyond conventional voltage and temperature monitoring. Rapid EIS and gas sensors have demonstrated strong potential to provide critical warning times of several minutes, enabling preventative action before hazardous events unfold. For LFP-based batteries, which are often considered safer due to their thermal stability, early detection remains essential, especially given the flammability of hydrogen-rich off-gases. As battery systems continue to grow in scale and complexity, the development of integrated, multi-modal diagnostics will play a central role in advancing battery safety.

In this study, we evaluate the performance of rapid EIS and commercial gas sensors as early warning diagnostics for LFP/Gr pouch cells subjected to thermal and electrical abuse. The investigation is conducted across four system configurations:

- single cell;
- one series, four parallel (1s4p) pack;
- four series, one parallel (4s1p) pack; and
- and a four parallel, two series (4p2s) pack.

Through in-operando testing, we characterize the onset of failure, warning time, and signal sensitivity for both diagnostic techniques under OT and OC conditions. The results are analyzed in the context of system complexity, cell-to-cell interaction, and abuse mode, providing insight into the scalability and limitations of each method. This work aims to inform the development of diagnostic strategies that can be integrated into next-generation battery management systems, with the goal of improving safety, reliability, and response time under high-risk conditions.

Experimental Methods

To evaluate the diagnostic tools and identify failure markers, cells were subject to abuse conditions via two pathways: OT and OC. Fifteen Ah LFP/Gr pouch cells (Tenergy, Item # 30208[2]) were used for testing either single cells, 1s4p, 4s1p, or 4p2s packs, where "s" indicates the number of cells in series, and "p" indicates the number of cells in parallel. Single cells and packs were assembled using phenolic or brass fixturing plates and corner bolts, hand-tightened to an estimated 10-25 N·m to secure the assembly without applying significant pressure to the cells. K-type thermocouples (TCs) (Omega, 36 gauge) were placed on each cell, and between fixturing plates and cell. For all tests, the cells were brought up to 100 percent state-of-charge prior to test initiation. Charging to 100 percent SOC was accomplished by using a constant current with a C-rate of 0.3 C until the cell reached 3.8 V, then applying a taper charge at a constant voltage of 3.8 V until the current reduced to C/20.

During all tests, the cells were connected to a rapid EIS system (Dynexus Technology, iRIS P1-02[3]). All EIS measurements were taken for the range of 0.1 Hz to 1638 Hz (the upper limit of the rapid EIS equipment is 2 kHz). EIS measurements during OC were taken at an interval rate of 5 percent SOC, while during OT, measurements were taken every 60 seconds. For diagnostic purposes, this report presents the time-resolved magnitude of impedance at 0.1 Hz, along with the full spectrum EIS data for each test. The failure marker was defined at the point when the first derivative of the impedance with respect to time changes sign from negative to positive.

Four gas sensors were mounted 58 cm ± 3 cm from the cell(s). Each sensor employs a different proprietary gas detection method. These sensors included two VOC gas detectors (VOC1 Li-ion Tamer, Part# 241022, and VOC2 developed by Idaho National Laboratory); a combined VOC, CO_2, and H_2 sensor (Metis Engineering, Part# CANBSSGEN1[4]); and an H_2 sensor (Amphenol, Part# AX221058[5]). The VOC detectors, consistent with EPA 40 CFR 51.100, which defines reactive VOCs relevant to ozone formation, output a digital signal received by a data acquisition system. Voltage sensing for all tests was also routed to the same DAQ. The combined gas sensor collects data in ppb for VOC, and in ppm for CO_2 and H_2, and transmits that data via controller area network bus where it was retrieved using a LabVIEW DAQ card and LabVIEW based software. The H_2 sensor employs a thermal conductivity detection method and outputs an analog signal, which is collected using a LabVIEW DAQ card and LabVIEW-based software. The function of each gas sensor was validated prior to each test using acetone for VOC1, VOC2 and combined gas sensors, and helium for the H_2 sensor (helium and hydrogen have similar thermal conductivity). In addition, Fourier-transform infrared spectroscopy was continuously operated (Thermo Fisher Scientific, Nicolet iS50[6]). The FTIR uses a gold KBr beam splitter with a process flow rate of 500 cm^3/min. The failure marker for gas detection was defined as the activation of each respective sensor represented as a drop in voltage for the VOC1 sensor, or an increase in the analog voltage signal for the VOC2, combined gas, and H_2 sensors.

Thermal runaway initiation via OT was carried out by fixturing either a single cell or a 1s4p pack between two brass plates (each 15.2 cm x 10.2 cm x 0.1 cm thick). Two cartridge heaters (Tutco

[2] Tenergy Power, Fremont, CA.
[3] Dynexus Technology Inc., Moscow, ID.
[4] Metis Engineering Ltd, Gloucestershire, England.
[5] Amphenol Corporation, Wallingford, CT.
[6] Thermo Fisher Scientific Inc., Waltham, MA.

Part# CH11456,[7] 300 W, 15.2 cm in length, 0.6 cm diameter) were placed on one brass plate (see Figure 1) to examine the effect of targeting thermal runaway in one side of the cell or in one cell within a pack (the cell adjacent to the heated brass plate). During all OT tests, the temperature ramp rate was controlled to 5°C/min using a proportional-integral-derivative (PID) controller. The PID loop is fed a temperature from a K-type TC that resides between the brass plate and battery cell, positioned at the center of the cell to keep the temperature ramp rate constant. Note that this TC reading is not saved and is therefore not reported in this work. The same TCs were used throughout all testing, including the OC-initiated thermal runaway tests. The TCs were first wrapped in a single layer of polyimide electrically insulating tape (Kapton). Then the TC was placed in the specified location using an additional layer of Kapton tape. This prevents TCs from slipping out of place during test assembly and operation.

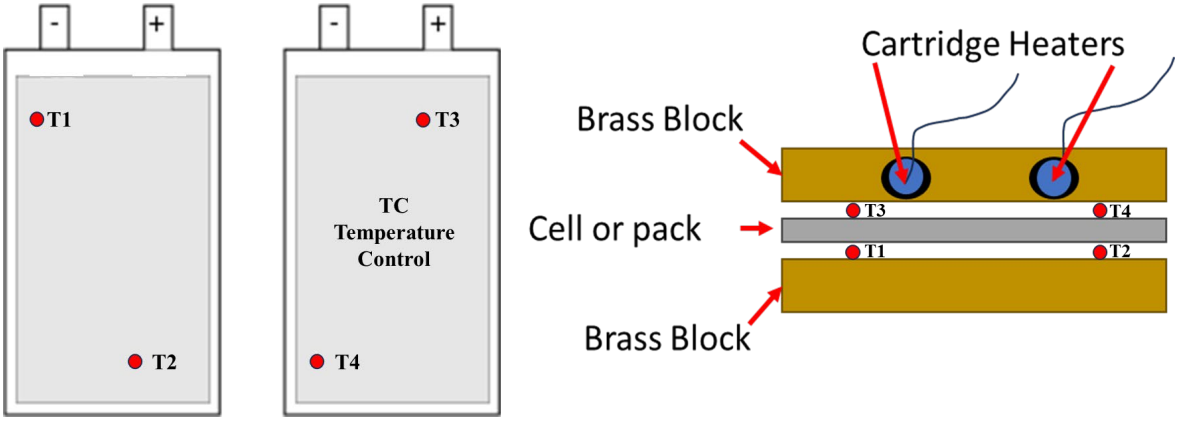

Figure 1. Schematic of the test setup for a single cell OT test

Failure initiation via OC was carried out by fixturing a single cell, 1s4p pack, or 4s1p pack between two phenolic resin plates (15.2 cm x 15.2 cm x 1.3 cm thick). Phenolic plates are used for OC because they are thermally insulating. This better replicates conditions that are relevant to a scenario where cells are placed in packs and/or casing that does not have the conductive heat transfer that would occur with metal fixturing plates (e.g., brass plates). The unit under test was then connected to a power supply (Hewlitt Packard PN# 6032A, 0 to 50 A, 1000 W) to supply the current necessary for the OC condition. In this work, all cells were charged to 100 percent SOC **prior to the start of the OC test.** The OC condition was held at 1C until cell failure was observed. The capacity was 15 Ah for both the single cells and the 4s1p configuration, while the capacity for the 1s4p pack was 60 Ah.

[7] Tutco Heating Solutions Group, Cookeville, TN.

Results and Discussion

This study evaluates the effectiveness of rapid EIS and commercially available gas sensors for early warning detection of LFP/graphite cells. Both techniques were tested under thermal (OT) and electrical (OC) failure conditions. Key metrics included the onset temperature for thermal failure and the onset SOC for electrical failure. Failure onset was defined as the point where the cell heating rate exceeded 6° C/min, indicating a greater heating rate compared to that provided by the heater. In cases where thermal runaway was observed, failure was classified as the onset (T or %SOC) of thermal runaway. Additional metrics include the time of sensor activation ($S_{\text{activation time}}$), the time of failure onset (cell-HR_{time}), and the warning time ($\Delta t_{\text{warning time}}$). The warning time was calculated using the equation below.

$$\Delta t_{warning\ time} = cell\text{-}HR_{time} - S_{activation\ time}\ \#$$

OT and OC testing were conducted with four distinct gas sensors: VOC1, VOC2, combined gas, and H_2. During these tests, the dynamics of gas evolution were captured via FTIR, while electrochemical changes were assessed with rapid EIS (iRIS) either every 60 seconds for OT tests or every 5 percent SOC for OC tests. Concurrently, voltage and temperature measurements were recorded throughout the testing process. The in-operando testing methodology involved real-time data acquisition while the target cell was subjected to abusive conditions. The placement of gas sensors was an important factor, positioned at a defined path length of 58 cm ± 3 cm from the unit under test, while the FTIR system operated over a significantly longer path length, on the order of several meters. This difference in path lengths led to a minor but quantifiable delay in the FTIR response relative to the gas sensors. However, this delay, typically on the order of less than 30 seconds, was sufficiently minimal to ensure FTIR data remained closely aligned with real-time gas sensors measurements. The data presented here provides a comprehensive view of gas evolution kinetics, highlighting critical temporal correlations between gas emissions, electrochemical changes, and thermal behavior under OT and OC conditions.

Overtemperature Failure Initiation

Figure 2 through Figure 14 show the results of OT testing conducted using an in-operando testing methodology. This approach involved real-time data acquisition while the target cell was subjected to a controlled heating rate of 5° C/min, applied to one side of the cell until failure conditions (i.e., cell-HR > 6° C/min) were met. The testing protocol was systematically applied across various configurations, including single cells, 1s4p, and 4p2s arrangements. This testing framework enabled a thorough examination of the cell's performance and behavior under the specified thermal conditions.

Overtemperature Failure in Single Cells

Figure 2(a) presents the voltage and temperature profiles recorded during OT testing of an LFP/Gr pouch cell. The cell surface temperature, measured by TCs T3 and T4 positioned on the side in direct contact with the heating element, showed a continuous rise throughout the test, reaching a peak temperature of 250° C (testing limit). Around 20 minutes into the test (at approximately 130° C), a subtle, short-lived temperature plateau was observed, which also manifested as a sudden decrease in the cell-HR, as shown in Figure 2(b). This could indicate the occurrence of a minor vent. Such mild vent, while not visibly detectable, may reduce contact

between the cell and the heating surface, temporarily decreasing local heat transfer efficiency (Feng et al., 2018).

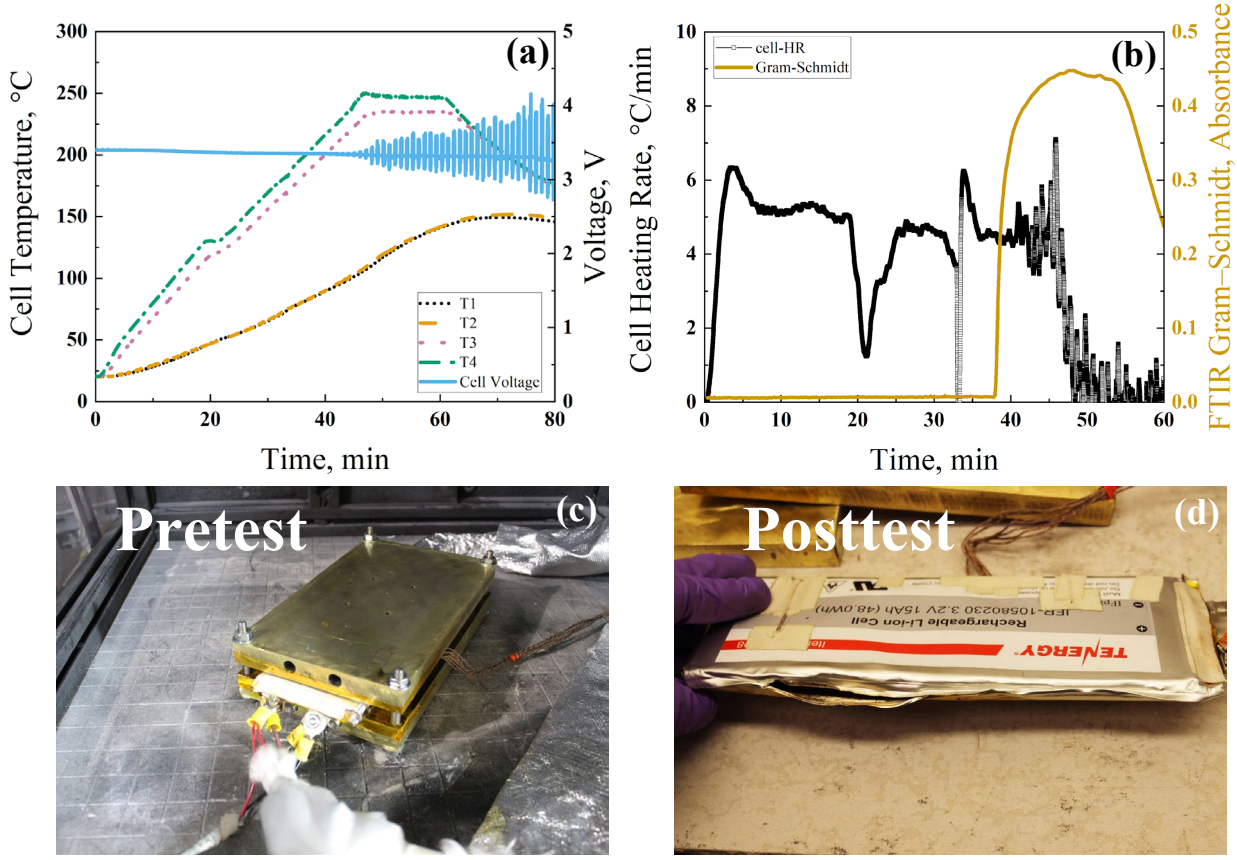

Figure 2. Temperature and voltage response of a single cell during OT testing. (a) Temperature and voltage, (b) cell heating rate and time resolved FTIR measurements, (c) pretest images and (d) posttest images.

Video footage captured during the test revealed continuous swelling of the cell over the first 20 minutes, which then momentarily plateaued before resuming and culminating in visible venting, electrolyte leakage, and rupture of the cell (see pretest and posttest images in Figure 2). This progressive swelling behavior is consistent with gas generation due to electrolyte decomposition and SEI breakdown, which are among the earliest thermal degradation processes in LFP/Gr cells (Kvasha et al., 2018; Shen et al., 2023). The temporary stagnation in swelling may reflect partial gas release or redistribution within the cell layers. However, no thermal runaway was observed, which aligns with the known high thermal stability of LFP cathodes. LFP materials lack the oxygen-release characteristics of higher-nickel chemistries and thus are less prone to self-sustaining exothermic reactions (Barkholtz et al., 2019; Khakani et al., 2016). Therefore, the onset of failure was the point where the cell-HR exceeded 6° C/min [Figure 2(b)], occurring at approximately 170° C. This inflection point may correspond to accelerated degradation reactions, such as SEI decomposition and the onset of electrolyte vaporization, which could lead to a measurable change in thermal response. Due to limited thermal conductivity across the cell thickness, thermocouples positioned on the side of the cell opposite to the heater recorded lower temperatures, reaching a maximum temperature of ~152° C. This thermal gradient is expected in

such configurations and reflects anisotropic heat transfer, which may contribute to localized degradation zones within the cell during abuse conditions.

Voltage measurements remained relatively stable throughout the test, with only a minimal drop (~15 mV), suggesting that the cell retained electrochemical functionality until late in the abuse test. The most prominent voltage deviations were transient and coincided with rapid EIS measurements, rather than being thermally induced. However, as the test progressed and the cell experienced increased thermal stress, these EIS-related perturbations became more pronounced. This behavior is attributed to an increase in internal cell resistance, likely caused by the breakdown of interfacial layers (e.g., SEI and electrode/electrolyte interfaces), gas evolution disrupting ionic pathways, and changes in electrolyte conductivity. These are characteristic signatures of early-stage thermal failure in LFP/Gr cells, and while they did not escalate to thermal runaway, they signify a transition into a thermally unstable state.

Time-resolved FTIR measurements were conducted in parallel with commercial gas sensors to enable a detailed analysis of gas evolution. The results are shown in Figure 2(b), where the cell-HR is overlaid with the FTIR Gram Schmidt total absorbance spectra. This overlay allows for correlation between thermal events and gas evolution signatures, helping to identify the point when vented gases begin to escape from the cell. The initial FTIR signal related to gas generation, primarily from electrolyte decomposition, was detected shortly after venting. The calculated FTIR $\Delta t_{\text{warning time}}$ was -4.1 minutes, indicating that FTIR did not provide advance warning. This delay is attributed to two key factors: (1) the absence of a thermal runaway event in this particular test and (2) the detection threshold for calculating warning time being defined by a specific cell-HR, rather than onset to thermal runaway. Consequently, the quantity of evolved gas was initially too low to register a significant FTIR response, as the detection path length and dilution effects delay the time at which sufficient gas reaches the FTIR detector.

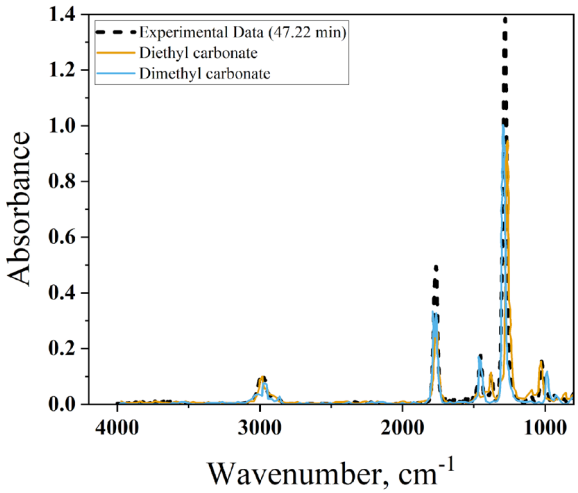

Figure 3. FTIR spectrum at 47.2 min (peak absorbance) for a single cell during OT testing

The maximum FTIR total absorbance (~0.45 from Figure 2(b)) occurred at 47.2 minutes after the start of the test, which corresponds to the peak in gas evolution. This delay reflects the gradual accumulation of off-gassed species, primarily due to decomposition of the organic carbonate electrolyte solvents. The FTIR spectrum at this time, shown in Figure 3, was dominated by features characteristic of diethyl carbonate and dimethyl carbonate, consistent with known decomposition pathways of common lithium-ion battery electrolytes (Golubkov et al., 2014).

Although the FTIR did not provide advance warning prior to the cell-HR threshold, the large increase in detected gas concentrations after this point suggests that significant off-gassing can occur even in the absence of thermal runaway. In LFP/Gr cells, the release of gases such as VOCs and CO_2 can continue for extended periods post-venting, driven primarily by ongoing electrolyte decomposition (Golubkov et al., 2014). The continued buildup of flammable and potentially toxic gases in a confined space may still pose serious risks, including the potential for delayed ignition or pressure buildup.

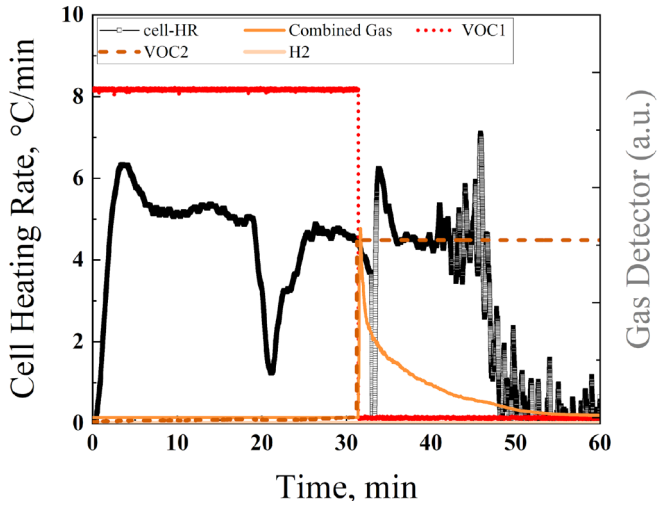

Figure 4. Response of commercial gas sensors during single cell OT testing

The response profiles of the gas sensors are presented in Figure 4. All sensors designed to detect VOCs, including VOC1, VOC2, and the combined-gas sensor, activated shortly before the determined cell-HR threshold (>6° C/min). VOC1 and the combined-gas sensor each provided a $\Delta t_{warning\ time}$ of 2.1 minutes, whereas VOC2 yielded a slightly extended $\Delta t_{warning\ time}$ of 2.5 minutes. These sensors are sensitive to a range of low molecular weight hydrocarbons and carbonate decomposition products released during the early stages of thermal abuse. The primary sources of these VOCs include the evaporation and initial thermal degradation of organic electrolyte solvents (Figure 3), such as ethylene carbonate, dimethyl carbonate, and ethyl methyl carbonate, which typically begin to decompose below 160° C (Golubkov et al., 2014; Lamb et al., 2015; Pasquier et al., 1998; Qiu et al., 2023; Sun et al., 2016; Yang et al., 2004; Yuan et al., 2020). These reactions occur prior to significant structural breakdown of the electrode materials and serve as precursors to more severe failure mechanisms.

In contrast, the H_2 sensor did not exhibit a detectable response during the OT test and therefore provided no warning time. Although LFP/Gr cells are recognized for their improved thermal stability and comparatively lower gas evolution rates, numerous studies have shown that they still generate hydrogen during abuse conditions (Shen et al., 2023; Golubkov et al., 2015). Hydrogen evolution in LFP/Gr cells occurs primarily via reductive decomposition of electrolyte solvents at the lithiated graphite anode, as well as catalytic reactions involving trace metal impurities, separators, or binder breakdown at elevated temperatures. Despite this, the concentration of hydrogen generated in this test may have remained below the sensor's minimum detection threshold of 8,000 ppm. Other contributing factors may include limited gas transport to the sensor, suboptimal sensor placement relative to the vent path, or the kinetics of hydrogen

release. In this context, hydrogen kinetics refers to the rate at which hydrogen is generated and disperses within the enclosure.

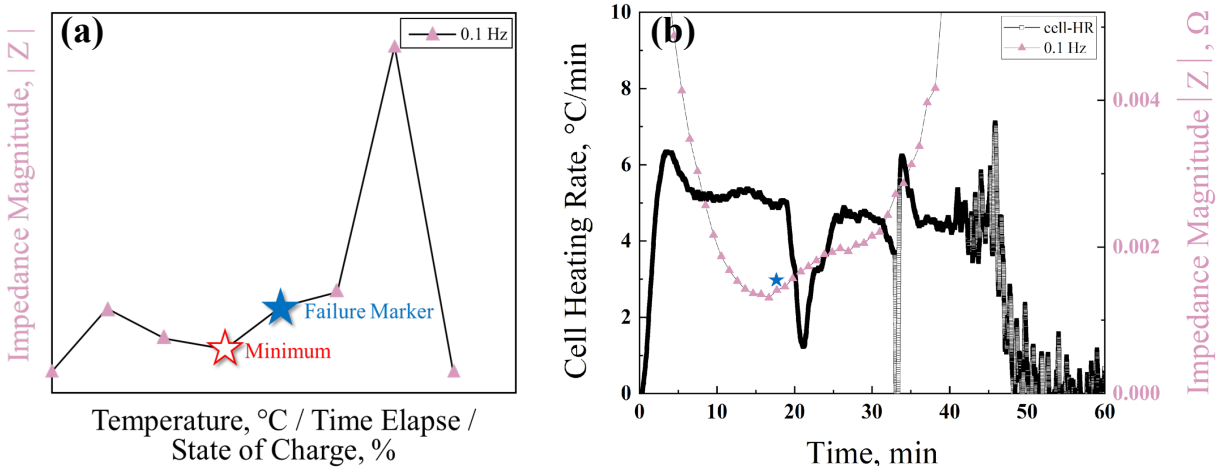

Figure 5. Impedance magnitude at 0.1 Hz during OT testing of a single cell. (a) Qualitative graphical representation of rapid EIS failure marker (solid blue star) during abusive conditions, and (b) impedance magnitude at 0.1Hz.

Electrochemical diagnostics using rapid EIS were conducted concurrently. A general trend observed across lithium-ion batteries under thermal abuse is a transient decrease in internal resistance as temperature increases. This phenomenon is well understood in the context of thermally enhanced electrochemical kinetics: higher temperatures accelerate lithium-ion transport and reduce charge transfer resistance at the electrode-electrolyte interface. Additionally, elevated temperatures increase the ionic conductivity of the electrolyte. As a result, cells may exhibit temporarily improved impedance characteristics despite being in an energetically unstable regime. However, this regime is short-lived; continued heating initiates irreversible degradation processes, including SEI breakdown, gas evolution, and electrolyte decomposition. These effects collectively drive a subsequent rise in impedance and signal the onset of internal failure.

In this report, rapid EIS (0.1 Hz- 1638 Hz) was employed to monitor these electrochemical transitions in real time. Figure 5(a) presents a qualitative representation of this characteristic failure pattern. The minimum in impedance magnitude, marked with a red open star, corresponds to the point of maximally improved kinetics, where internal resistance is temporarily minimized due to favorable temperature-induced transport and reaction conditions. The failure marker, indicated by a solid blue star, is defined as the point immediately following this minimum, where impedance begins to increase. This upward trend reflects the onset of irreversible cell degradation, particularly due to SEI decomposition and parasitic reactions at the anode interface (Dong et al., 2021; Feng et al., 2018; Lyu et al., 2022; Torres-Castro et al., 2024). Figure 5(b) shows the evolution of the impedance magnitude at 0.1 Hz, extracted from full EIS spectra captured every 60 seconds. This low-frequency region was selected due to its high sensitivity to interfacial kinetics and lithium-ion diffusion processes, two indicators of cell stability. Notably, changes in impedance began to appear at temperatures as low as 55 °C (see Figure 6 for temperature resolved patterns). In LFP/Gr cells, this early response likely comes from the thermal instability of the SEI layer on graphite, which begins to degrade and reform at relatively

modest temperatures. This process increases interfacial impedance even in the absence of gas generation.

Analysis of the full EIS spectra (Figure 6) further revealed the appearance of a diffusion tail. Interestingly, in some cases, the diffusion tail displayed a reversed or backward-bending shape, an atypical feature that suggests deviation from ideal Warburg-type diffusion. Such distortion may be caused by evolving internal resistances, gas formation, or changes in porosity and tortuosity due to electrode degradation. As the electrolyte structure and transport pathways become disrupted, classical semi-infinite diffusion assumptions no longer apply, leading to non-ideal impedance behavior. The failure marker defined by the post-minimum impedance increase was observed at ~108 °C, which offered a 16-minute warning time. The ability to detect degradation early highlights the sensitivity of EIS to internal chemical and structural instabilities. In contrast to gas sensors, which respond only when volatile degradation products are released, EIS enables detection of precursory electrochemical shifts, providing a significantly earlier warning. In this case, EIS offered over six times more lead time compared to gas-based diagnostics. Nonetheless, applying this diagnostic technique in larger battery packs (e.g., 1s4p or 4p2s) presents new challenges.

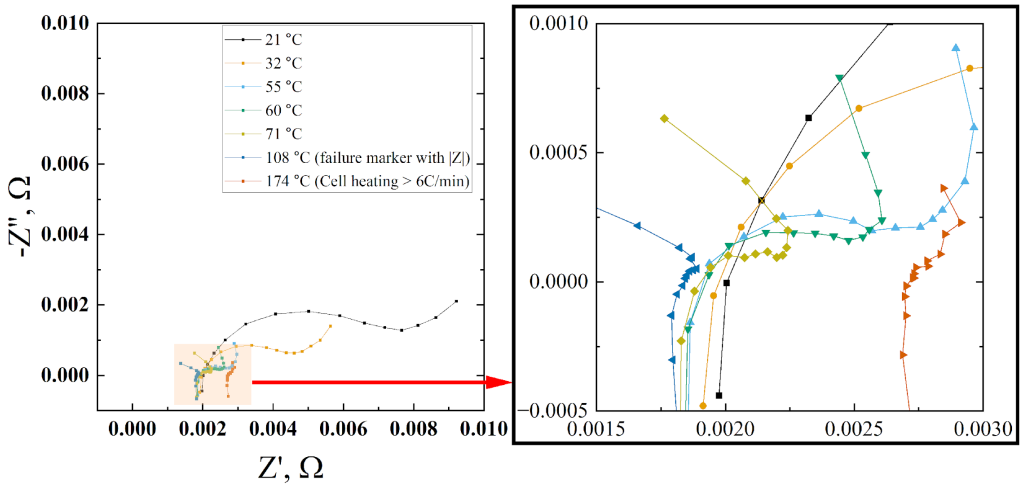

Figure 6. Nyquist plots at various temperatures during the single cell OT test. This also includes the failure marker plot from Figure 5 and the plot at the failure threshold (cell-HR > 6° C/min).

Overtemperature Failure in a 1s4p and 4p2s Pack Configuration

While single-cell experiments offer controlled conditions for isolating specific failure mechanisms and evaluating diagnostic sensitivity, real-world battery systems operate in interconnected formats where cells influence each other thermally, electrically, and chemically. These interactions can mask or alter diagnostic signals, making direct extrapolation from single-cell data insufficient. As such, validating diagnostics techniques at the pack level is crucial for ensuring their effectiveness under practical conditions. Scaling introduces additional complexities, including current redistribution, nonuniform heating, and interconnect resistance, all of which can significantly impact the onset, propagation, and detection of failure events (Zhang et al., 2018; Li et al., 2023; Naylor Marlow et al., 2024; Wu et al., 2013).

To evaluate how diagnostic responses scale with both parallel and series connectivity, two pack configurations were investigated: a 1s4p and a 4p2s, both constructed using the same 15 Ah

LFP/Gr pouch cells. The 1s4p pack had a nominal capacity of 60 Ah and a maximum operating voltage of 3.4 V, while the 4p2s configuration maintained the same capacity but doubled the operating voltage to 6.8 V. In the 1s4p configuration, a brass plate was affixed directly to the cell stack, and OT conditions were initiated by applying localized heating to the edge-most cell (cell 1) using two embedded cartridge heaters. In the 4p2s configuration, only one of the two strings was affixed to a brass plate and heated, while the second string was placed adjacent to it without direct heating (Figure 11). Gas sensors were positioned 58 cm ± 3 cm from cell 1 to monitor volatile species evolution while pack-level voltage measurements tracked the electrochemical response. Rapid EIS was conducted at 60-second intervals to capture time-resolved changes in impedance as a function of thermal exposure and electrical interconnection.

1s4p Pack Configuration Response

Figure 7 shows (a) the temperature and voltage profile for the 1s4p pack configuration, (b) the TC placement, and (c) the HR profile of B1-C1 (the TC located between Cell 1 and the heater block. Cell 1, which was directly heated, exhibited clear signs of venting at approximately 122° C, 22 minutes after the start of heating. This is indicated by a distinct inflection in the HR profile, characterized by a sharp rise followed by a transient decrease (Figure 7(c)). After venting, the cell continued to heat, with failure (cell-HR > 6° C/min) occurring at 228° C. The cell reached a maximum temperature of 250° C (testing limit) without triggering thermal runaway.

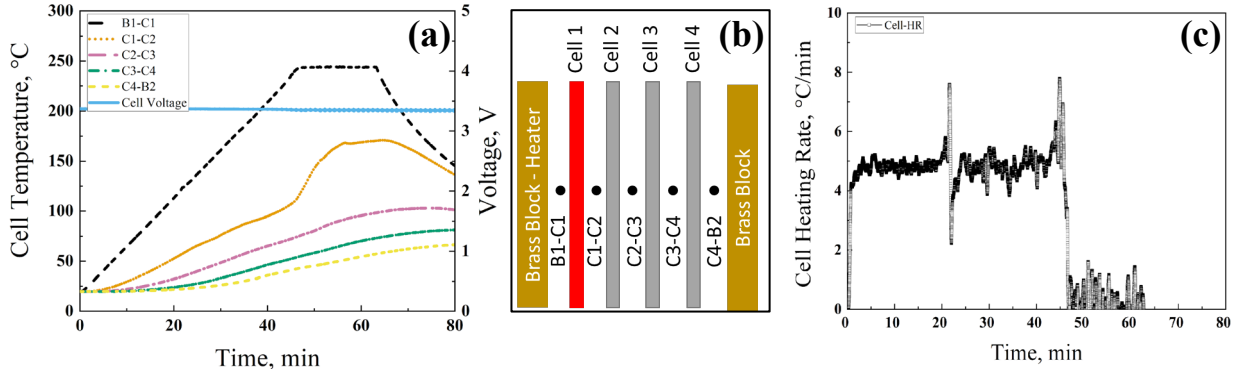

Figure 7. Temperature and voltage response during the OT test of a 1s4p pack. (a) The temperature and voltage profile for the 1s4p pack configuration, (b) the TC placement, and (c) the HR profile of B1-C1 during the test.

In the sequence of failure events, minor electrolyte leakage was detected shortly after venting. This leakage is characterized by a small, controlled release of electrolyte fluid that does not immediately compromise the integrity of the system but serves as an early indicator of failure. This was subsequently followed by the release of light smoke and a significant gas release at the failure point. Figure 8 overlays the FTIR Gram-Schmidt signal with the cell-HR, showing a strong temporal correlation between gas evolution and thermal response. Both the single-cell and the 1s4p configurations exhibited a similar peak FTIR absorbance of 0.45, indicating comparable maximum gas concentrations. This similarity suggests that gas generation primarily occurred from the failure of cell 1, with no propagation to adjacent cells. As a result, the total gas volume and species concentration remained comparable to that of the single-cell event. However, the 1s4p pack showed a more sustained absorbance signal, suggesting prolonged gas release. This is likely influenced by thermal coupling between adjacent cells, which facilitates heat distribution

across the pack. The heat generated by the failure of one cell can be transferred to neighboring cells, leading to a more uniform temperature distribution. This may reduce peak temperatures in the initially affected cell, promoting a slower decomposition process and extending the duration of volatile emissions.

This delayed and more gradual gas evolution also corresponds with a higher failure onset temperature of 228° C in the pack, compared to 170° C in single-cell tests. In isolated cells, heat remained confined, causing a rapid local temperature rise and earlier activation of exothermic reactions. In contrast, the greater thermal mass and interconnected structure of the pack likely enhanced heat dissipation and delayed the rise in local temperatures. While this difference may have resulted from heat redistribution and increased thermal mass in the stacked configuration, other factors such as measurement variability, differences in venting dynamics, or mechanical constraints like cell compression may also have played a role. These system-level thermal effects are important when extrapolating single-cell behavior to larger battery assemblies and should be considered when designing safety diagnostics.

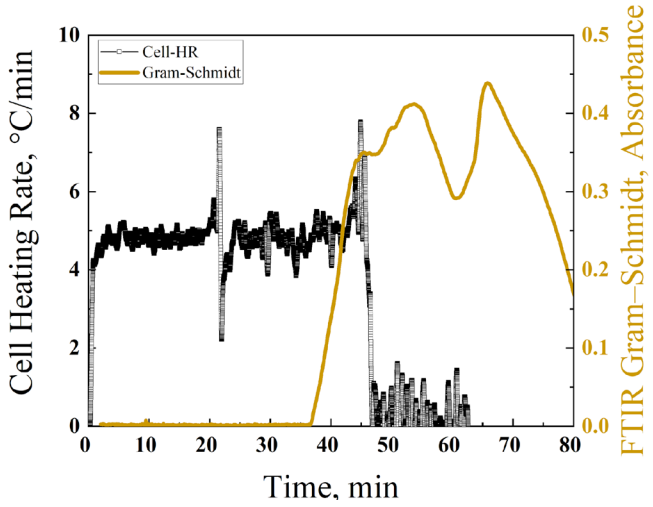

Figure 8. Cell heating rate and time-resolved FTIR during the OT test of a 1s4p pack

Figure 9(a) shows the gas sensor measurements for the 1s4p pack configuration. The VOC2 and combined-gas sensors triggered simultaneously during the initial venting event of cell 1, indicating early detection of volatile species. In contrast, VOC1 and H_2 gas sensors did not trigger during the test, likely due to difference in sensor detection dynamics such as gas-specific sensitivity, response thresholds, or kinetics. Warning time ($\Delta t_{warning\ time}$) was defined as the interval between gas sensor trigger and the point at which the HR of cell 1 exceeded 6° C/min. The VOC2 and combined-gas sensors provided a $\Delta t_{warning\ time}$ of 15.4 and 15.2 minutes, respectively. Neither the VOC1 nor H_2 sensors provided measurable warning time in this configuration. In comparison to single-cell tests, which had warning times of 2.5 minutes for the VOC2 sensor and 2.3 minutes for the combined-gas sensors, the pack exhibited longer warning times. The greater thermal mass and enhanced heat dissipation pathways in the pack delayed the transition from venting to failure, providing additional time for gas-based diagnostics to respond.

These results highlight the influence of pack design on diagnostic performance, particularly for gas sensors. In multicell systems, vent-path geometry, internal airflow, and cell-to-sensor distance all affect how quickly and reliably gas species reach detection points. In the 1s4p configuration, venting from cell 1 may have followed a longer or more distributed path

compared to single-cell setups, enabling earlier detection by some sensor while delaying or preventing the activation of others.

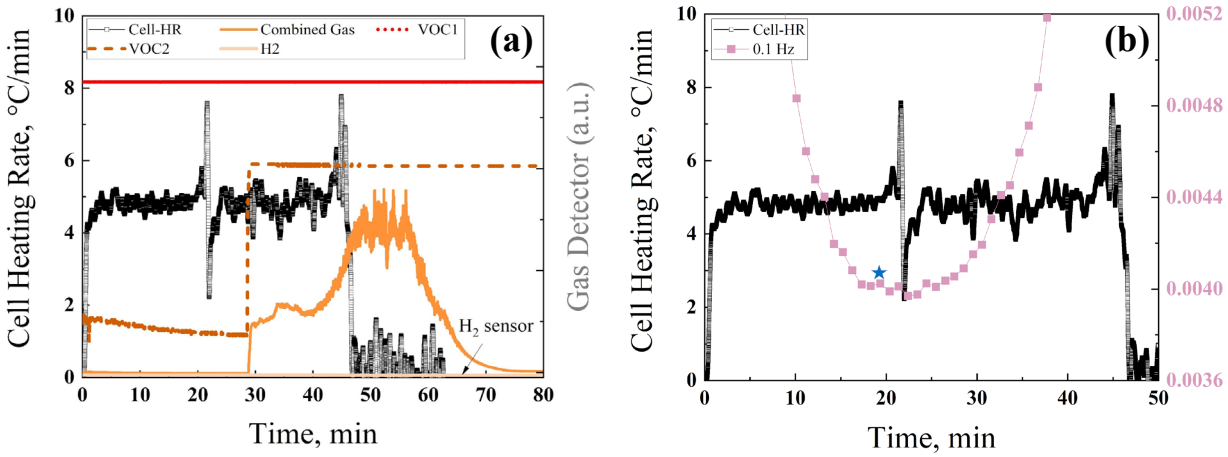

Figure 9. (a) Gas sensor response and (b) impedance magnitude at 0.1 Hz during OT testing of a 1s4p pack

Rapid EIS was employed to capture time-resolved electrochemical changes during the test, with the 0.1 Hz frequency magnitude shown in Figure 9(b) as a representative signal. Although only this frequency is plotted for clarity, full-spectrum EIS data were collected at various time points and are presented Figure 10. In the rapid EIS profile, a subtle plateau in impedance magnitude was observed prior to failure, with the threshold identified at 110° C. Using this point as the failure marker, the $\Delta t_{\text{warning time}}$ was calculated to be 24.6 minutes.

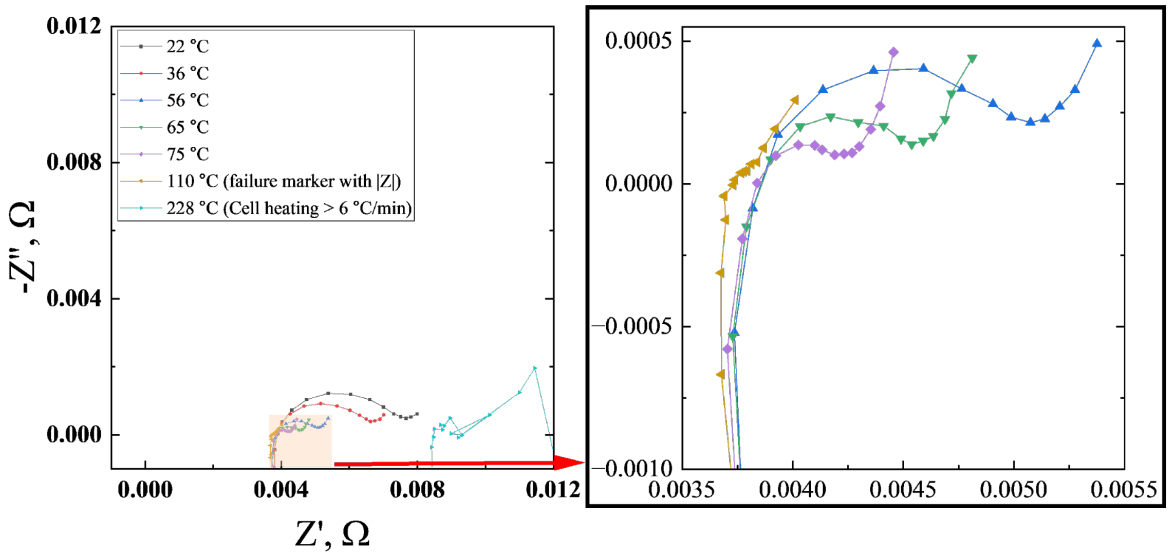

Figure 10. Nyquist plots at various temperatures during the 1s4p OT test. This also includes the failure marker plot from Figure 9(b) and the plot at the failure threshold (cell-HR > 6° C/min).

While the underlying principles of impedance response to early-stage degradation have been described in detail in an earlier section, it is worth noting that EIS offered a significantly longer warning time in this configuration compared to gas sensors. However, applying EIS at the pack level introduces new challenges. As system complexity increases, impedance signals tend to become less distinct due to averaging across two or more cells and potential interference from wiring and interconnects. This is evident when comparing the rapid EIS data from the 1s4p pack (Figure 9(b)) with those from the single-cell test (Figure 5(b)). The change in impedance between the minimum and failure marker (blue star) was only $1.05 \times 10^{-5}\ \Omega$ in the pack, compared to $1.03 \times 10^{-4}\ \Omega$ in the single cell. Similarly, Nyquist plots in Figure 10. show minor changes in the full pack during early degradation, whereas the single-cell data (Figure 6) exhibit more pronounced shifts. These differences reflect not only the averaging effect across cells but also the increased complexity of the equivalent circuit at the pack level.

4p2s Pack Configuration Response

Following the evaluation of sensor response in single cells and a 1s4p pack, we examined the added complexity of a mixed configuration with a 4p2s pack. Figure 11 presents the temperature profile (a), voltage response (b), TC placement (c), and experimental setup (d) for the OT test conducted on this configuration. In contrast to the single-cell and 1s4p tests, where thermal runaway was not observed, the 4p2s configuration exhibited full-pack failure. Cell 1 underwent thermal runaway at approximately 196° C, reaching maximum temperatures > 600° C. As shown in Figure 11(a), the event propagated through the entire pack, consuming both parallel strings within approximately 20 minutes. The voltage profile in Figure 11(b) shows that the string containing the triggered cell experienced a rapid voltage drop within seconds of the thermal runaway onset. The adjacent string began to degrade approximately 5 minutes later, indicating delayed but eventual propagation of failure. Although the propagation rate was slower than typically observed in higher-energy chemistries such as lithium nickel manganese cobalt oxide or lithium cobalt oxide, the onset and spread of failure in an LFP-based system (known for its thermal stability) raises important concerns on scalability (Torres-Castro et al., 2020).

Several factors may have contributed to the onset of thermal runaway in the 4p2s configuration. The addition of a second series string effectively doubled the pack voltage while maintaining the same parallel structure, increasing the total energy available to sustain thermal reactions once initiated. Higher voltage could also contribute to more aggressive current redistribution during abnormal conditions, potentially leading to localized overstress. However, as shown in the temperature profile (Figure 11), Cell 2 entered thermal runaway almost simultaneously with Cell 1, suggesting minimal delay in propagation and highlighting the strong thermal and electrical coupling between cells. Given that this configuration resulted in thermal runaway, two failure criteria are used to assess sensor warning time ($\Delta t_{\text{warning time}}$): (1) the point at which the cell-HR exceeded 6° C/min, and (2) the onset of thermal runaway.

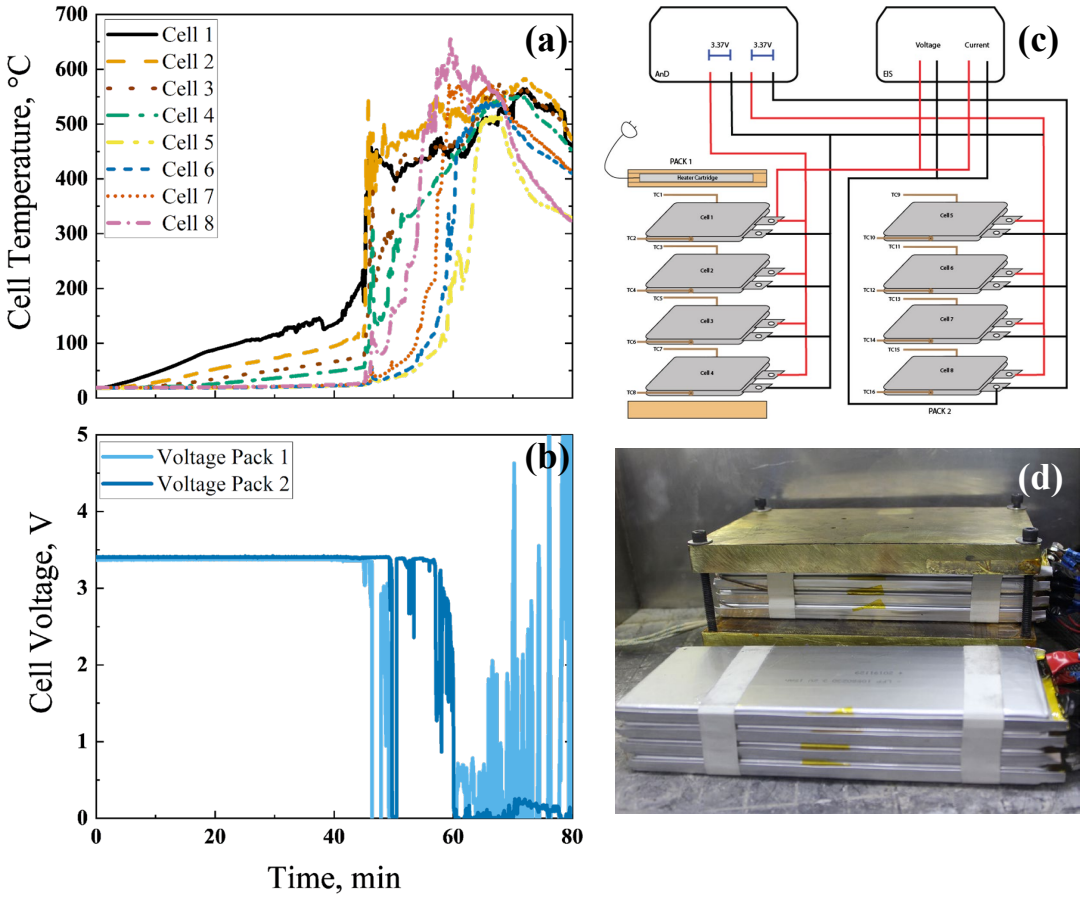

Figure 11. Temperature and voltage response of a 4p2s pack during the OT test. (a) Temperature and (b) voltage response during the OT test of a 4p2s battery pack. The pack configuration is shown in (c), along with the experimental setup image in (d).

Video footage of the test shows initial swelling of the failed cell, followed by light smoke emission from a minor vent in the pouch casing. After several minutes, the cell vented at a higher gas release rate, quickly filling the test enclosure with dense smoke. Ignition of the gases occurred shortly afterward, producing a flame jet directed toward the polycarbonate viewing panel, which subsequently melted. Although polycarbonate is often cited as having a melting point of 230° C, it is an amorphous polymer and does not really have a sharp melting point like crystalline materials. Instead, it has a glass transition temperature near 147° C and softens progressively when exposed to elevated temperatures. The intensity and duration of the hot gases and flames were sufficient to deform and melt the panel, as well as damage other components inside the test enclosure. Figure 12 shows posttest images highlighting the melted polycarbonate cover and damaged aluminum parts, providing visual confirmation of the extreme thermal conditions sustained during the event.

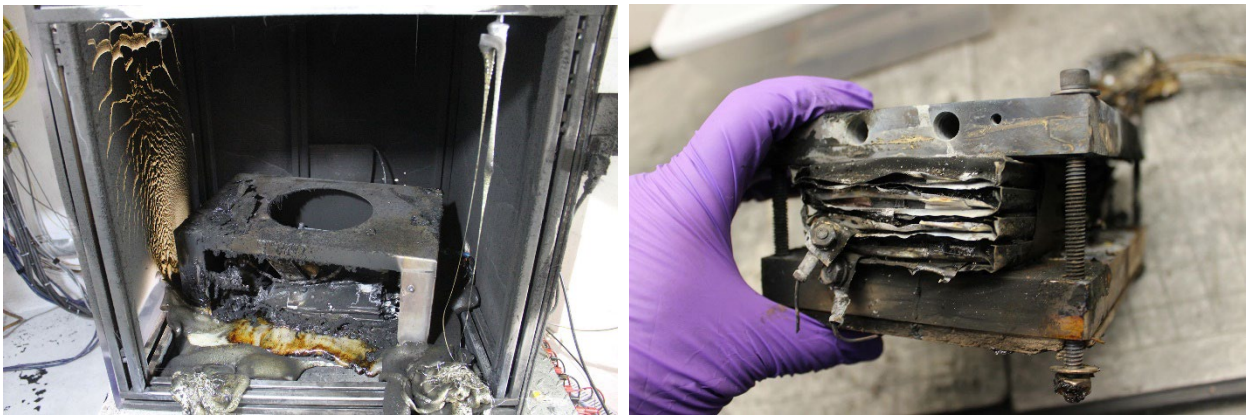

Figure 12. Post-overtemperature images of the 4p2s LFP/graphite battery pack

Figure 13 shows the gas sensor measurements for the 4p2s pack configuration. Using failure criterion 1, defined as the point at which cell-HR exceeded 6° C/min, only VOC2 and combined-gas sensors triggered. VOC2 provided a $\Delta t_{warning\ time}$ of 2.6 minutes, similar to what was observed in single-cell testing, while the combined-gas sensor offered a slightly longer $\Delta t_{warning\ time}$ of 6.2 minutes. When applying failure criterion 2, defined as the onset of thermal runaway, all gas sensors were activated due to the volume of gas release during the event. However, not all sensors provided advanced warning. For example, VOC1 triggered after thermal runaway, resulting in a negative $\Delta t_{warning\ time}$ of -0.03. VOC2 and the combined-gas sensor again provided the longest $\Delta t_{warning\ time}$, at 16.5 and 20.0 minutes, respectively. The H_2 sensor, consistent with prior findings in the literature, triggered shortly before thermal runaway, yielding a modest $\Delta t_{warning\ time}$ of 0.3 minutes.

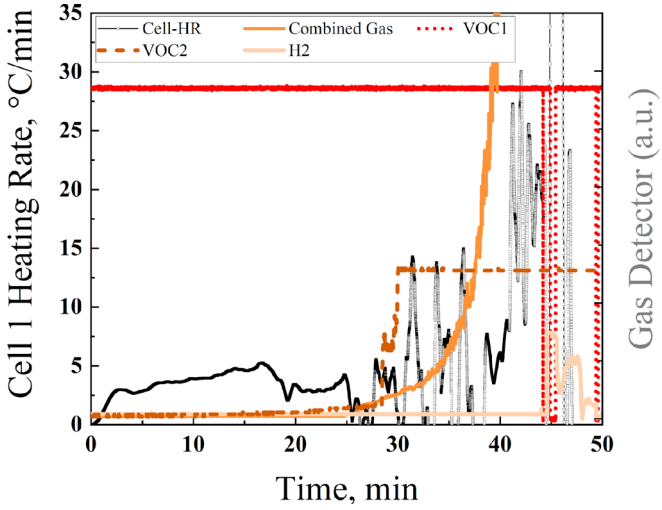

Figure 13. Gas sensors response during the OT test of a 4p2s pack

The electrochemical changes during the test are represented by the 0.1 Hz frequency magnitude shown in Figure 14(a) and the full-spectrum EIS data presented in Figure 14(b). In the rapid EIS profile, a steady decrease in impedance magnitude was observed over the first 35 to 38 minutes of the test. A sharp increase in impedance occurred at 130.2° C, which was identified as the failure marker. Using failure criterion (1), defined by a cell-HR > 6° C/min, rapid EIS did not

provide early warning. However, when applying criterion (2), defined as the onset of thermal runaway, rapid EIS yielded a warning time of 5.9 minutes. The reduced sensitivity of rapid EIS under criterion (1) highlights a key limitation of the technique as pack complexity increases. As more cells and interconnections are added, the electrochemical response of the failing cell can become masked by the averaged behavior of the system. This is further supported by the Nyquist plots at different temperature points in Figure 14(b), where the typical semicircular shape does not show significant change until higher temperatures (around 130° C) when the failure was ultimately detected. These results suggest that, while rapid EIS remains a valuable diagnostic tool, its effectiveness in complex, multicell configurations may be limited without advanced localization or signal filtering strategies.

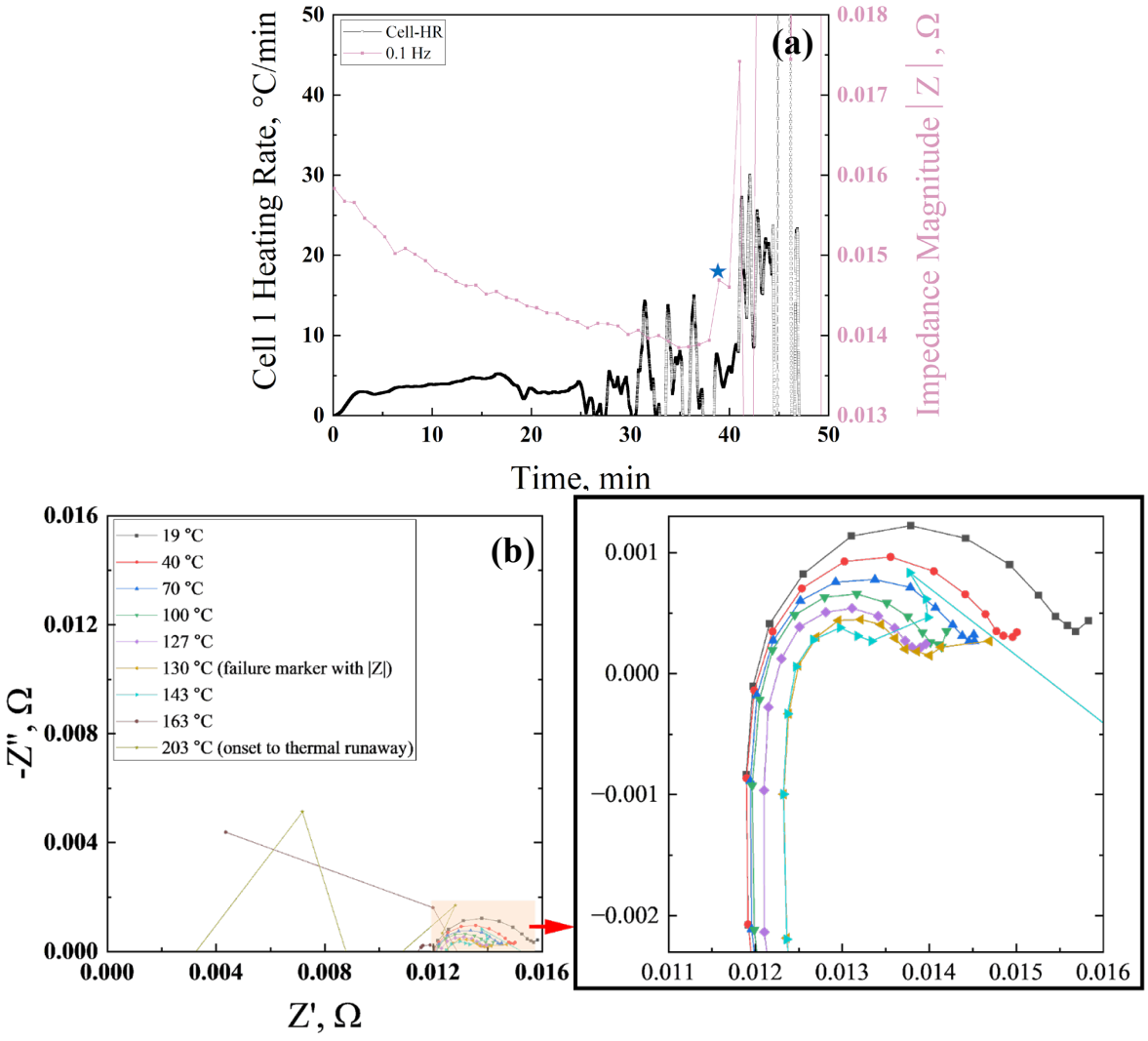

Figure 14. (a) Impedance magnitude at 0.1 Hz and (b) Nyquist plots at various temperatures during the 4p2s OT test

The OT tests across the single cell, 1s4p, and 4p2s configurations reveal how battery architecture fundamentally influences failure dynamics and the effectiveness of diagnostic strategies. While the single-cell and 1s4p setups remained stable under test conditions, the 4p2s configuration experienced full-pack thermal runaway, highlighting how increased voltage, energy density, and thermal coupling can compromise the inherent thermal stability of LFP chemistry. As shown in Table 1, warning times varied significantly across configurations and diagnostics, with gas sensors such as VOC2 and the combined-gas sensor generally providing the most consistent early indicators of failure. Electrochemical impedance, though valuable in simpler systems, showed reduced sensitivity in more complex pack-level tests due to signal averaging and masking effects.

Table 1. Δtwarning time for single cell and pack level testing during OT conditions (single data points)

Cell Configuration	Sensor	$\Delta t_{warning\ time}$ (min)
Single cell	iRIS	16.0
	VOC1	2.3
	VOC2	2.5
	Combined Gas	2.3
	H_2	No detection
1s4p (OT of cell 1)	iRIS	24.6
	VOC1	No detection
	VOC2	15.4
	Combined Gas	15.2
	H_2	No detection
4p2s (OT of cell 1) $\Delta t_{warning\ time}$ calculated based on failure criterion 2	iRIS	5.9
	VOC1	-0.03
	VOC2	16.5
	Combined Gas	20.1
	H_2	0.3

Overcharge Failure Initiation

Figure 15 to Figure 26 show results of OC testing across different LFP/Gr configurations, including single cells, 1s4p, and 4s1p arrangements. Each test involved subjecting the cell to a 1C constant current until either 250 percent SOC or failure. Real-time measurements, including voltage, temperature, current, and gas evolution, were collected throughout the overcharging process. Rapid EIS was also conducted at 5 percent SOC intervals to capture internal resistance changes as the cell progressed toward failure.

Overcharge Failure in Single Cells

The temporal evolution of cell temperature and voltage during the single-cell OC test is shown in Figure 15(a). Around 6 minutes into the test, an inflection point in the temperature profile

indicates the onset of accelerated self-heating. This shift is clearly reflected in the cell-HR, shown in Figure 15(b) along with the FTIR Gram-Schmidt overlay, and occurs after the cell reaches approximately 110 percent SOC at a temperature near 28° C. Visual observations confirmed significant cell swelling at this point, suggesting the onset of internal gas formation and electrolyte decomposition.

Cell failure was defined as the point at which the cell-HR exceeded 6°C/min, occurring at approximately 132 percent SOC and a temperature of 74° C. Two additional inflection points in the temperature curve followed, indicating continued thermal activity. The voltage profile during OC exhibited characteristics typical of LFP/Gr cells under excessive charge conditions. After initial current application, the voltage response showed a small polarization of approximately 28 mV. This was followed by a steady increase in cell voltage up to 6 V, after which the voltage temporarily stabilized. As charging continued, the voltage approached the compliance limit of 20 V near 135 percent SOC. This behavior reflects increasing interfacial resistance due to potential lithium plating at the Gr anode. Overcharging leads to a shift in electrochemical reactions, often resulting in electrolyte oxidation, gas formation, and irreversible electrode damage. The plateau and subsequent voltage drift also indicate limitations in the cell's ability to accommodate additional lithium ions. Compared to chemistries like NMC or LCO, LFP is inherently less tolerant to OC. In LFP cells, nearly all lithium is extracted from the cathode at full charge. This makes the system more vulnerable to over-delithiation, which can destabilize the olivine structure, promote iron dissolution, and increase side reactions at the electrode–electrolyte interface. In contrast, layered oxides like NMC and LCO retain a fraction of lithium in the cathode after full charge, providing additional buffer before structural degradation begins.

Video footage captured during the test showed continuous swelling within the first 10 minutes (up to 115% SOC). A slight decrease in cell volume was later observed, which is likely the result of a minor venting event, though no vent was visually confirmed. Light smoke became visible around 20 minutes (133%–135% SOC), several minutes after the failure point, followed by rapid gas generation and the accumulation of dense smoke in the lower section of the test enclosure. Although gas evolution and venting occurred, there was no evidence of thermal runaway or gas ignition. Posttest inspection, shown in Figure 15(d), revealed no visible signs of mechanical failure, rupturing, or casing breach, despite the internal degradation processes observed during testing.

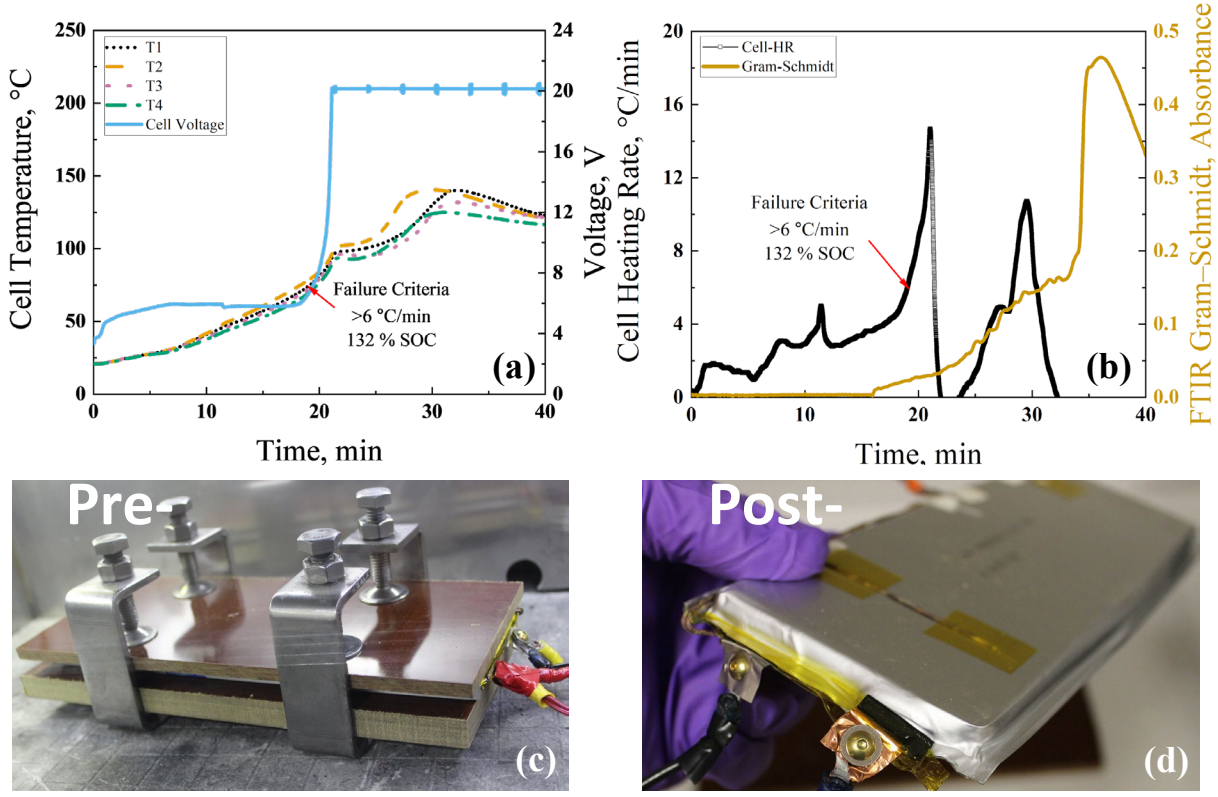

Figure 15. Temperature and voltage response of a single cell during OC testing.
(a) *Temperature and voltage response, (b) cell heating rate and time resolved FTIR measurements, (c) pretest images and (d) posttest images.*

Time-resolved FTIR spectroscopy in Figure 15(b) is overlaid with the cell-HR to serve as a reference parameter. The first detection of a gas signal occurred at 127 percent SOC, slightly before the appearance of light smoke in the test footage. This detection likely corresponds to the release of non-visible gases during a minor venting event, which is believed to have occurred between 115 percent and 120 percent SOC. The FTIR signal continued to rise, reaching its maximum absorbance approximately 36 minutes after the start of the test. The corresponding FTIR spectrum at that point is shown in Figure 16, with a peak absorbance of 1.5. Spectral fitting revealed the presence of carbonate-based electrolyte solvents, specifically DEC and DMC, consistent with decomposition of the electrolyte under OC conditions. The FTIR system provided a Δtwarning time of 2.9 minutes based on the defined failure point.

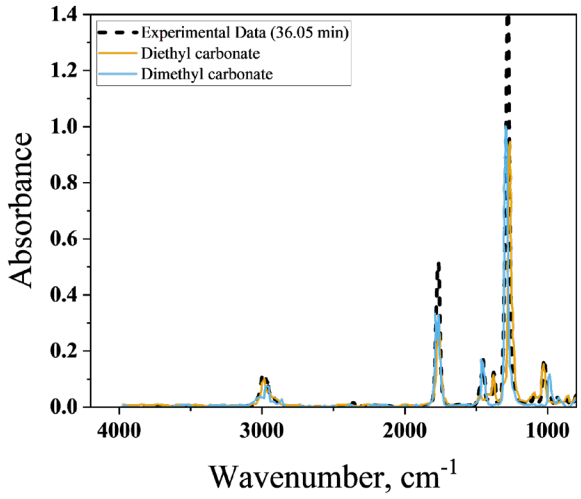

Figure 16. FTIR spectrum at 36.05 min (peak absorbance) for a single cell during OC

VOC1, VOC2, and the combined-gas sensor displayed significantly faster response times. As shown in Figure 17, all three sensors triggered at approximately 116 percent SOC, within seconds of each other. This timing coincided with the swelling event observed in the test footage, though no visible smoke was present at that stage. The $\Delta t_{warning\ time}$ provided by VOC1, VOC2, and the combined-gas sensor were 9.9, 9.7, and 9.8 minutes, respectively, substantially earlier than the FTIR detection. The faster activation of the gas sensors compared to FTIR can be attributed to differences in detection principles and system configuration. Gas sensors are point-based detectors located closer to the venting site and are highly sensitive to even low concentrations of VOCs. In contrast, the FTIR system relies on integrated path spectroscopy, which depends on the accumulation and distribution of gas in the optical path. As a result, FTIR often detects gases once concentrations are higher or more uniformly distributed across the sensing volume. While the detection principles are a primary factor in the observed differences in response times, other aspects, such as sensor placement and sensitivity, may also play a role.

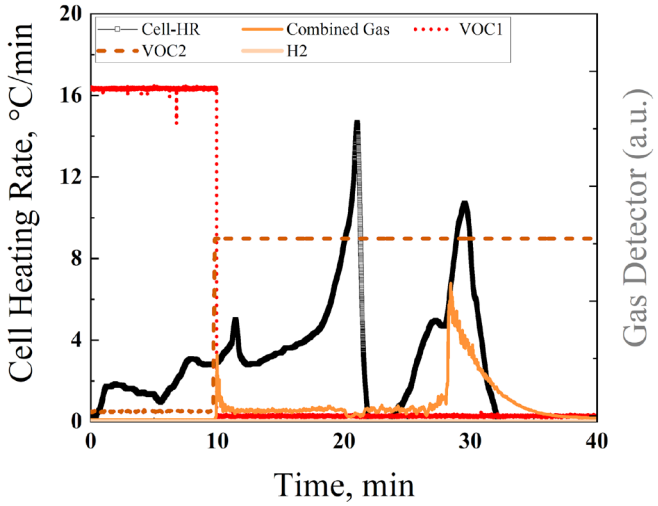

Figure 17. Response of commercial gas sensors during the OC test of a single cell

Figure 18(a) shows the impedance magnitude response at 0.1 Hz during the OC test. To avoid artifacts associated with the transition from open circuit to applied current, the EIS measurement taken at 100 percent SOC was excluded when selecting a failure marker. At that stage, impedance behavior is dominated by polarization effects from load activation rather than meaningful degradation. Instead, a more representative marker of imminent failure was identified at 128 percent SOC, where the impedance magnitude showed a distinct rise. This point was used to calculate a $\Delta t_{\text{warning time}}$ of 2.3 minutes. Full-spectrum EIS data, presented in Figure 18(b), reveal progressive changes across the frequency domain with increasing SOC. Notably, the Warburg tail, which is associated with diffusion-controlled processes, becomes increasingly elongated as the cell approaches failure. This elongation suggests a rise in lithium-ion transport resistance, likely due to lithium plating on the anode and the accumulation of insulating byproducts at the electrode–electrolyte interface. These effects slow ion diffusion, particularly in the low-frequency regime, and are indicative of severe electrochemical imbalance and growing internal resistance.

In this test, the rapid EIS $\Delta t_{\text{warning time}}$ of 2.3 minutes was significantly shorter than that of the gas sensors. These results suggest that, under OC conditions, the gas sensors were more effective in providing early warning than impedance measurements.

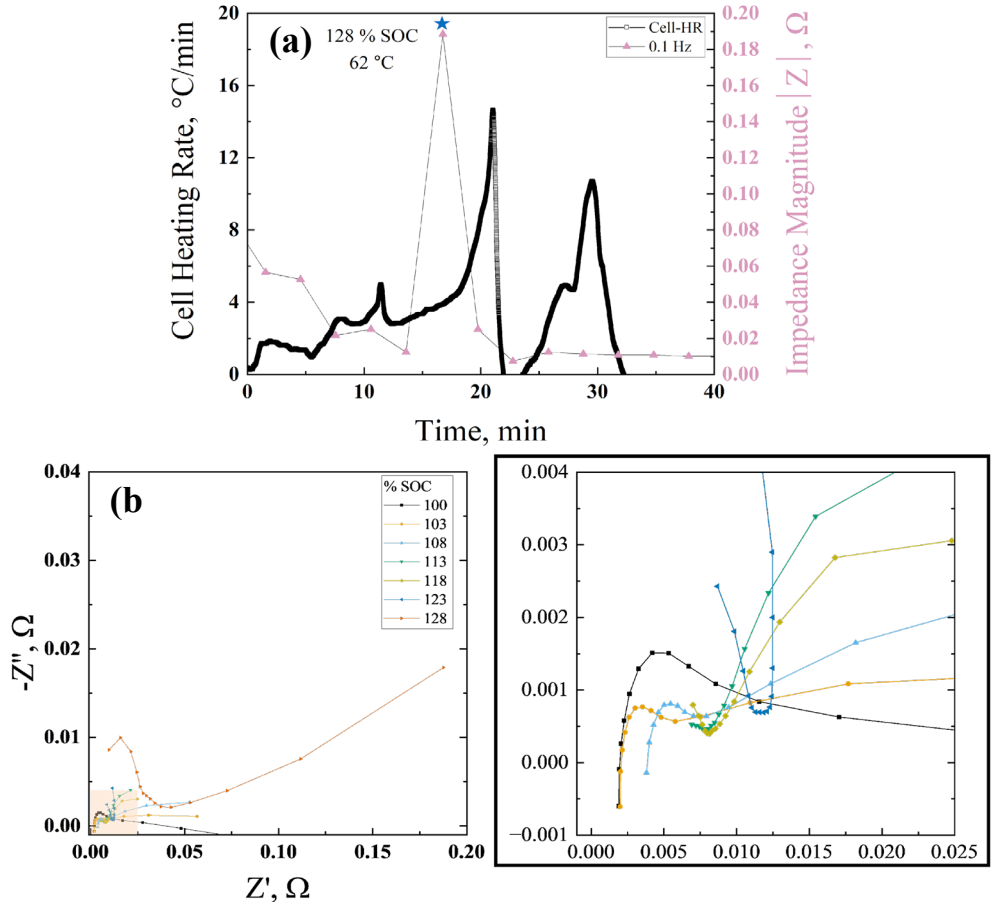

Figure 18. (a) Impedance magnitude at 0.1 Hz and (b) Nyquist plots at various temperatures during the single cell OC test

Overcharge Failure of a 1s4p and 4s1p Pack Configuration

OC failures in lithium-ion batteries involve complex, interdependent mechanisms that can evolve differently in multicell configurations compared to single cells. While single-cell testing allows clear identification of voltage polarization, gas generation, and internal resistance buildup, these signals can become less distinct at the pack level due to the influence of cell-to-cell interactions. In multicell systems, OC may lead to uneven current distribution, localized lithium plating, and accelerated degradation in certain cells, which can distort or delay diagnostic responses. Thermal and electrical coupling across cells further complicates detection, as early-stage failure signatures from one cell may be masked by the overall system response. To investigate how diagnostic behavior scales with both parallel and series connectivity, two pack configurations were tested: a 1s4p and a 4s1p layout. The 1s4p pack featured a nominal capacity of 60 Ah and a maximum operating voltage of 3.4 V, while the 4s1p pack maintained a nominal capacity of 15 Ah with a maximum operating voltage of 13.6 V. OC conditions were induced by applying a constant current of 60 A to the 1s4p pack with a compliance voltage of 20 V, and 15 A to the 4s1p pack with a compliance voltage of 60 V. Both configurations were mechanically constrained using phenolic plates to maintain structural integrity during the test. Gas sensors were positioned 58 ± 3 cm from the bottom of the stack to monitor the release of volatile species, and pack-level voltage was continuously measured to assess the electrochemical response under stress. Rapid EIS was performed at 5 percent SOC intervals throughout the charging process to track internal resistance evolution in real time.

1s4p Pack Configuration Response

Figure 19 presents the temperature and voltage profiles of the 1s4p pack configuration during the OC test (a), along with TC placement (b), pretest images (c), and posttest images (d). Similar to the single-cell OC test, an early inflection in the temperature curve was observed within the first 5 minutes, indicating the onset of mild self-heating. Between 9 and 11 minutes into the test, approximately 114 percent - 117 percent SOC, a more pronounced temperature rise occurred in several TCs, particularly the one located between cell 3 and cell 4 (TC: C3-C4). This TC was used to define the failure point, based on a cell-HR exceeding 6° C/min. As shown in Figure 21(a), the cell-HR sharply increased at this location, identifying failure onset at approximately 115 percent SOC and 55° C. This is significantly earlier than in the single-cell test, where failure occurred at 132 percent SOC and 74° C. The earlier onset in the 1s4p configuration may be attributed to increased heat generation and current redistribution within the parallel string, which can accelerate local degradation. The voltage behavior during the test followed a pattern similar to that of the single cell. After current application, the voltage immediately polarized and reached approximately 6 V before temporarily stabilizing. Continued charging led to a gradual increase until the compliance limit of 20 V was reached around 118 percent SOC.

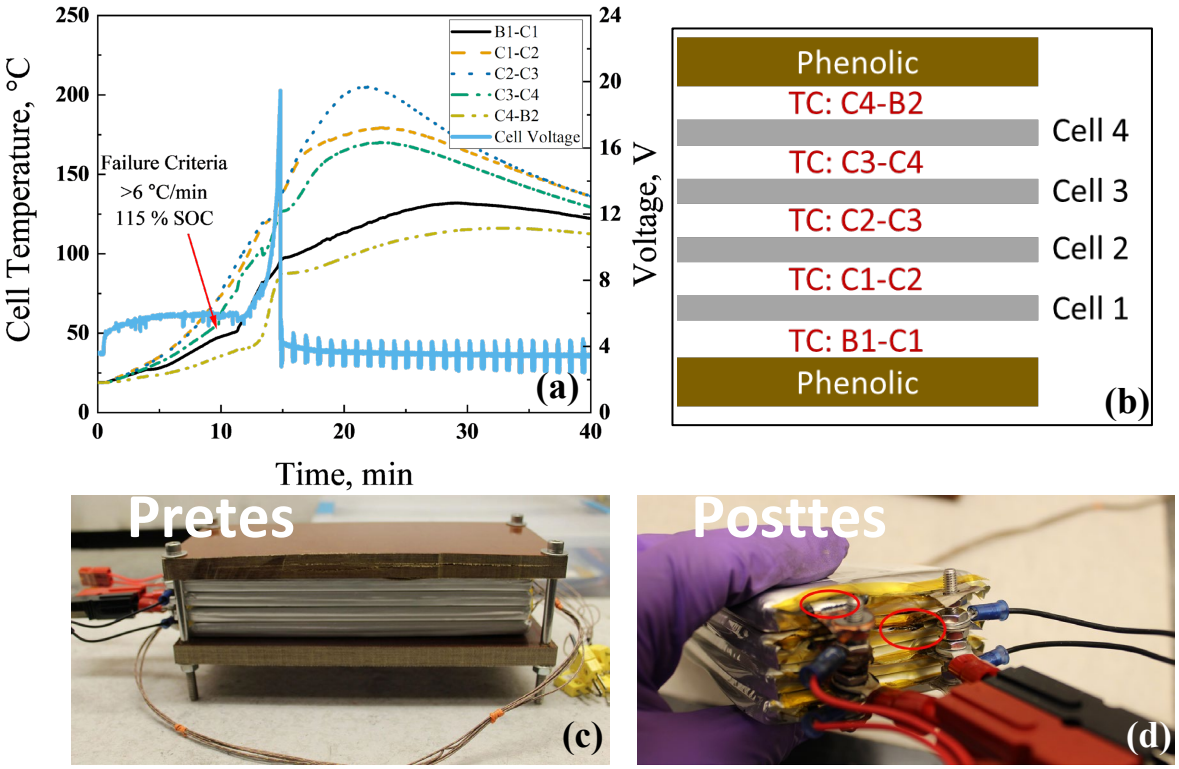

Figure 19. Temperature and voltage response of a 1s4p pack during the OC test. (a) Temperature and voltage, (b) a schematic representation of the unit under test, (c) pretest, and (d) posttest images.

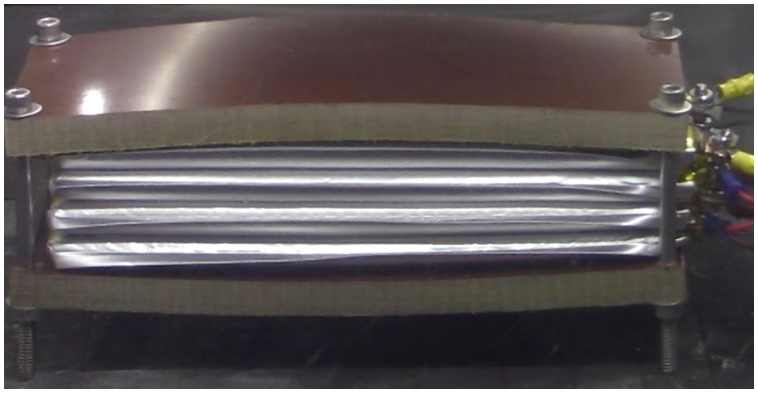

Figure 20. Still frame captured from the video of the 1s4p OC test

Video footage showed continuous cell swelling during the first 10 minutes, corresponding to SOC levels up to 116 percent. The swelling was substantial enough to visibly deform the phenolic blocks, as seen in Figure 20. This deformation may have restricted internal pressure relief, potentially intensifying localized heating and accelerating the onset of failure. Venting, electrolyte leakage, and light smoke followed shortly afterward, with rapid gas generation and dense smoke accumulation observed between 120 percent and 125 percent SOC (12 to 25 minutes into the test). Despite the significant gas release, there was no evidence of thermal runaway or flame ignition. Post-test inspection, shown in Figure 19(d), revealed dried electrolyte residue, minor burn marks, and casing breach, but no major structural damage.

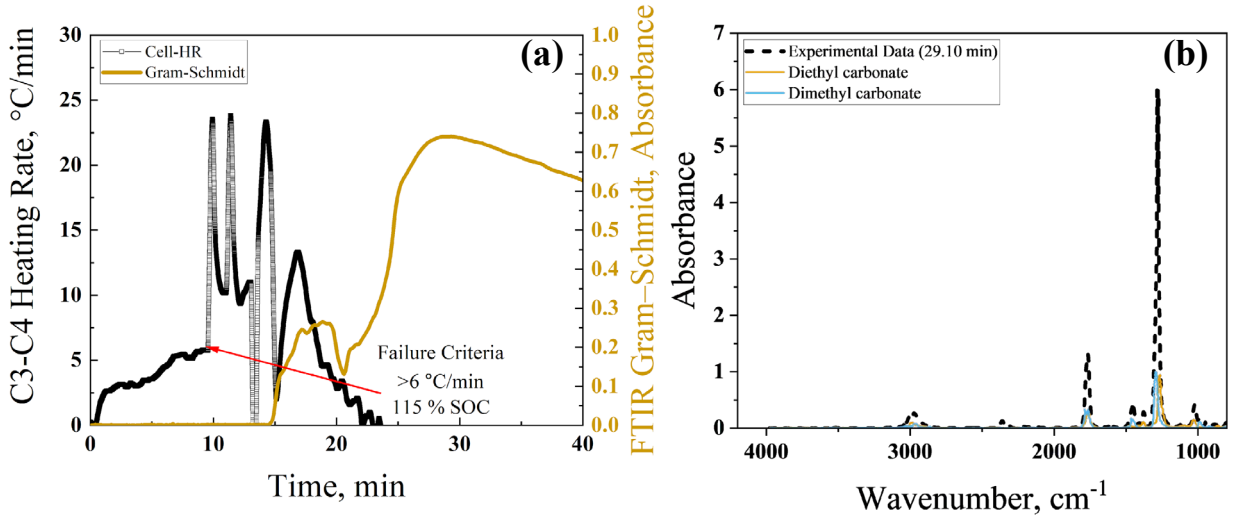

Figure 21. (a) Cell heating rate and time-resolved FTIR, and (b) FTIR spectrum at 29.10 minutes (peak absorbance) during the OC test of a 1s4p pack

Figure 21(a) displays the time-resolved FTIR Gram-Schmidt signal overlaid with the cell-HR. Gas detection via FTIR occurred at 124 percent SOC, aligning with the period of heavy gas release seen in the video. The signal peaked approximately 29 minutes after the start of the test, with the corresponding FTIR spectrum shown in Figure 21(b). A maximum absorbance of 6 was recorded, substantially higher than the peak absorbance of 1.5 observed during the single-cell test. This higher absorbance suggests greater gas concentration or a larger volume of evolved species in the 1s4p configuration, likely due to two or more cells contributing to the venting process. Despite this, FTIR detection occurred after the onset of failure, resulting in a negative $\Delta t_{\text{warning time}}$ of –5 minutes.

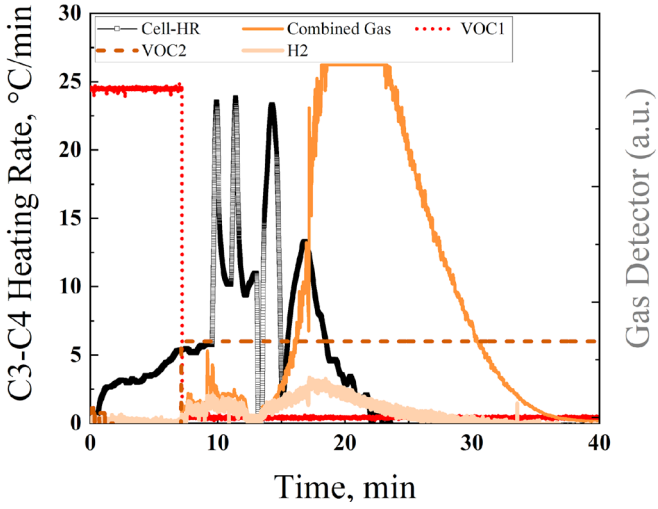

Figure 22. Response of commercial gas sensors during the OC test of a 1s4p pack

In contrast to FTIR, commercial gas sensors provided significantly earlier detection. As shown in Figure 22, VOC1, VOC2, and the combined-gas sensor all triggered at approximately 111 percent SOC, providing $\Delta t_{\text{warning time}}$ of 2.4, 2.2, and 2.4 minutes, respectively. Notably, the H_2 sensor also triggered during this test, while it remained inactive in the single-cell OC experiment. The activation of the H_2 sensor in the 1s4p configuration may be attributed to the increased severity of the event, resulting in higher concentrations of hydrogen-producing reactions. The involvement of two or more cells and potentially more extensive solvent decomposition could have produced sufficient hydrogen to surpass the detection threshold.

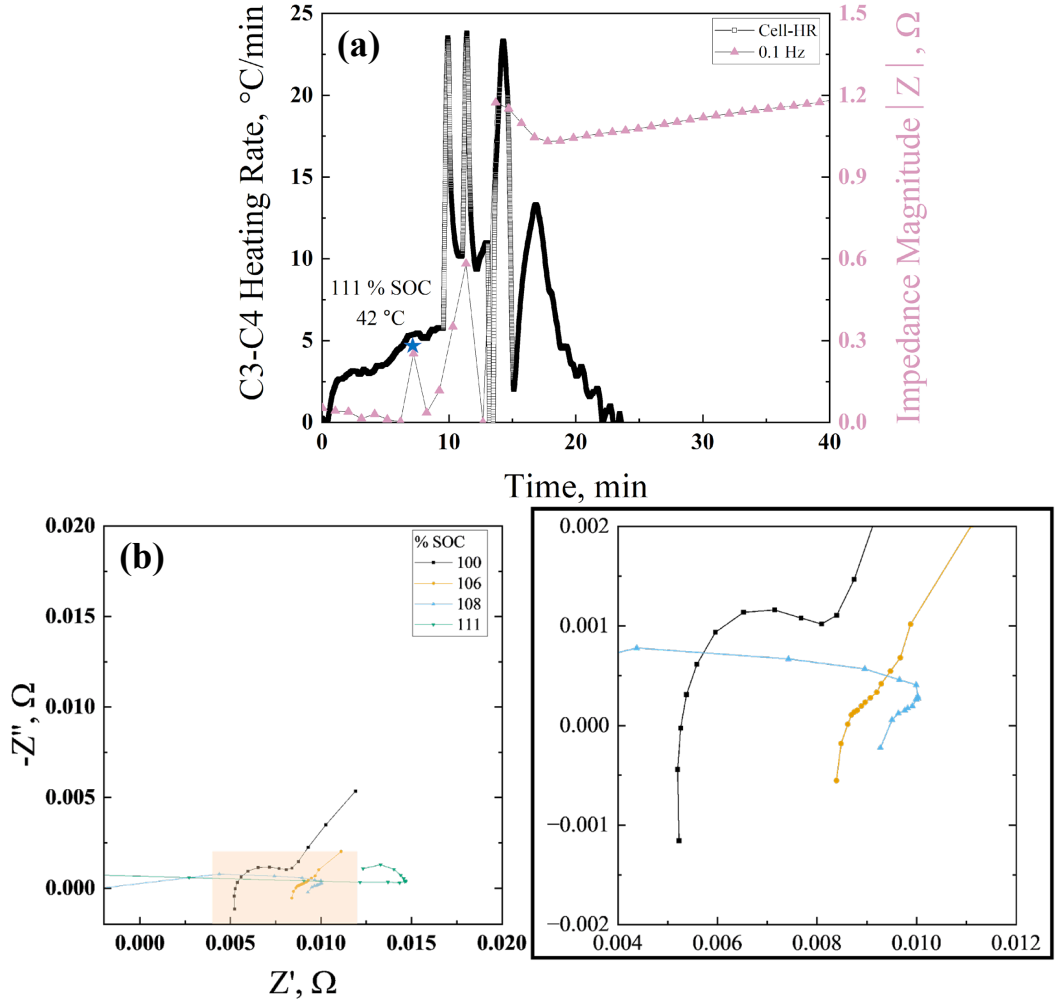

Figure 23. (a) Impedance magnitude at 0.1 Hz and (b) Nyquist plots at various temperatures during the 1s4p OC test

The impedance response during the OC test is shown in Figure 23(a), with the full Nyquist plot provided in Figure 23(b). A failure marker was detected at 111 percent SOC, resulting in a 2.4-minute warning window before the cell-HR exceeded 6°C/min. The full-spectrum EIS data exhibited elongation of the Warburg tail consistent with growing ion transport resistance, as also seen in the single-cell test. However, despite the failure marker appearing at a lower SOC than in the single-cell case, the earlier onset of thermal failure in the pack led to a shorter overall $\Delta t_{\text{warning time}}$. This reduction in $\Delta t_{\text{warning time}}$ when moving from single-cell to pack-level testing highlights the influence of system complexity. In multicell configurations, impedance signals tend to be

averaged across cells, which can mask localized degradation. Additionally, faster heat buildup and more constrained thermal dissipation reduce the time between initial signal detection and failure onset, narrowing the available window for intervention.

4s1p Pack Configuration Response

Following the single-cell and 1s4p OC evaluations, this section investigates diagnostic behavior in a 4s1p configuration, where cells are connected in series. Studying series-connected systems is essential for understanding how overcharge-induced failures evolve in higher-voltage packs, where cells are subjected to uneven voltage stress, greater potential for imbalance, and more constrained fault isolation. These conditions introduce unique challenges for both failure progression and diagnostic sensitivity, particularly when relying on electrochemical or gas-based signals for early warning.

The voltage and temperature responses are shown in Figure 24, along with a post-test image of the pack. The failure point, defined as the moment the cell-HR exceeded 6° C/min, was identified at 115 percent SOC and was used to calculate the $\Delta t_{warning\ time}$ for each diagnostic. During the test, cells 2 and 3 reached temperatures approaching 450° C. Despite these extreme temperatures, the extent of visible swelling was less severe than that observed in the 1s4p configuration. Clear signs of venting were recorded between 9 and 10 minutes into the test, around 115 percent to 116 percent SOC, with gases breaching the cell casing and significant electrolyte leakage occurring shortly after. Although substantial gas evolution was observed, no ignition occurred during the event. The post-test image in Figure 24 shows that the entire cell stack was burned, likely due to heat retention or smoldering that continued after the test ended.

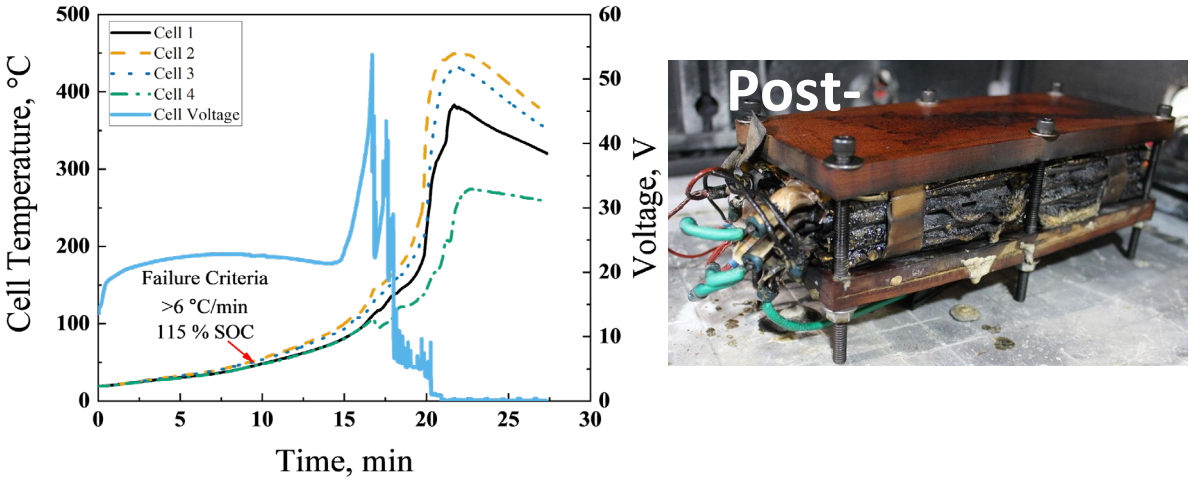

Figure 24. Temperature and voltage response during overcharge of a 4s1p LFP/Gr pack, and post-test image of the pack

Gas sensor responses during the test are shown in Figure 25. All sensors recorded strong signals, although their response times were not fast enough to provide meaningful early warning. The combined gas and H_2 sensors triggered at approximately 114 percent SOC, providing $\Delta t_{warning\ time}$ of 1.1 and 1.0 minutes, respectively. VOC1, however, activated much later, at 133 percent SOC, around 11.2 minutes after failure onset. This late response may be the result of a sensor malfunction or drift, rather than a true delay in gas presence. Issues such as sensitivity loss, obstruction of the gas path, or sensor aging could have affected performance. This highlights the

challenges of relying on a single gas sensor in practical systems, where environmental factors and placement can significantly impact detection reliability. Compared to earlier configurations, this test also showed shorter $\Delta t_{warning\ time}$ for gas sensors.

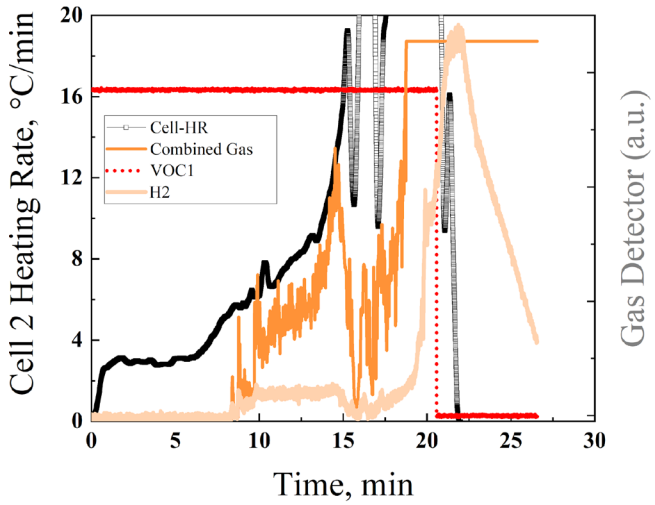

Figure 25. Gas sensor measurements during OC failure of a 4s1p LFP/Gr pack

The impedance response is presented in Figure 26(a), with corresponding full Nyquist plots shown in Figure 26(b). A failure marker was identified at 114 percent SOC and 48° C, resulting in a $\Delta t_{warning\ time}$ of only 0.7 minutes. This was the shortest $\Delta t_{warning\ time}$ observed for impedance-based diagnostics across all OC configurations tested. Compared to the 1s4p and single-cell tests, this result suggests that rapid impedance spectroscopy is less effective in detecting early-stage failure in series-connected systems. In these configurations, the electrochemical changes of a single cell are averaged with the rest of the pack, which reduces sensitivity to localized degradation. Additional factors such as SOC imbalance, unequal aging, and voltage redistribution further obscure electrochemical signatures, particularly under dynamic OC conditions.

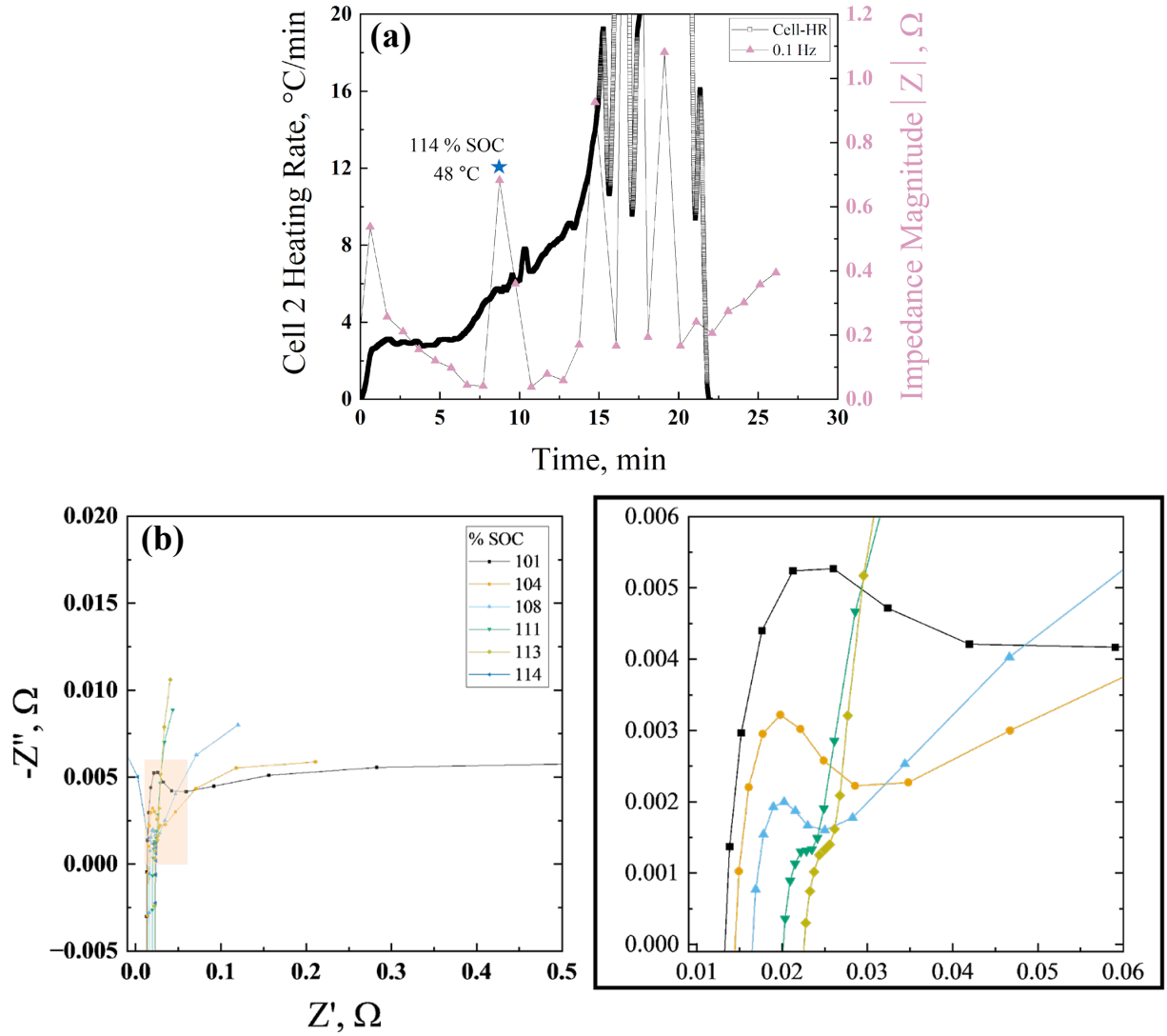

Figure 26. (a) Impedance magnitude at 0.1 Hz and (b) Nyquist plots at various temperatures during the 4s1p OC test

The OC tests demonstrate that as battery complexity and stored energy increase, the effectiveness of impedance-based diagnostics becomes increasingly constrained. The measured signal begins to wash out as system-level measurements average the behavior of multiple cells. This effect is especially clear when transitioning from the 1s4p to the 4s1p configuration, where early electrochemical indicators become less distinct and warning times decrease. While gas sensors were also affected by pack design and venting dynamics, they maintained more consistent detection performance, although their warning times were also reduced in the series-connected configuration. As shown in Table 2, the 4s1p pack produced the shortest warning times across all diagnostic methods tested during OC abuse. Although rapid EIS provided extended warning time in OT tests, it did not outperform gas sensors under OC conditions. This difference reflects the nature of OC failure, where resistance buildup and material degradation processes occur in close succession. In OT abuse, internal resistance changes can precede venting, allowing more time for detection and intervention. During OC, however, gas generation and structural

damage often begin before significant impedance shifts are measurable, compressing the available warning window

Table 2. Δtwarning time for 15 Ah LFP pouch cells during OC conditions: Cell and pack level testing (single data points)

Cell Configuration	Sensor	$\Delta t_{warning\ time}$ (min)	Sensor Triggered SOC (%)	Sensor Triggered T (°C)
Single cell	Combined Gas	9.3	116.3	39.3
	VOC1	9.1	116.5	39.7
	VOC2	9.4	116.1	38.8
	iRIS	2.3	128.0	62
	H_2	Not detected	Not detected	Not detected
1s4p	Combined Gas	2.4	111.1	41.4
	VOC1	2.4	111.2	41.6
	VOC2	2.5	111.0	41.0
	iRIS	2.4	111.2	41.6
	H_2	2.2	111.5	42.5
4s1p	Combined Gas	1.1	113.7	45.4
	VOC1	-11.2	133.9	429.5
	VOC2	Not used	Not used	Not used
	iRIS	0.7	114.4	47.7
	H_2	1.0	113.8	45.7

Intervention at Identified Failure Markers During Overtemperature Failure

The findings presented here demonstrate that gas sensors and rapid EIS are able to provide early failure detection in OT conditions. Next, we analyzed whether this early detection would give sufficient warning time for vehicle occupants to intervene and prevent adverse safety conditions. To explore this, an OT test was performed using the same setup and conditions described in earlier experiments. In this case, a thermal mitigation response was simulated by deactivating the heating element once either a gas sensor triggered, or a failure marker was detected via EIS. The removal of the heat source allowed the pack to cool passively through convective heat transfer to the ambient environment, serving as a simplified proxy for an active mitigation system.

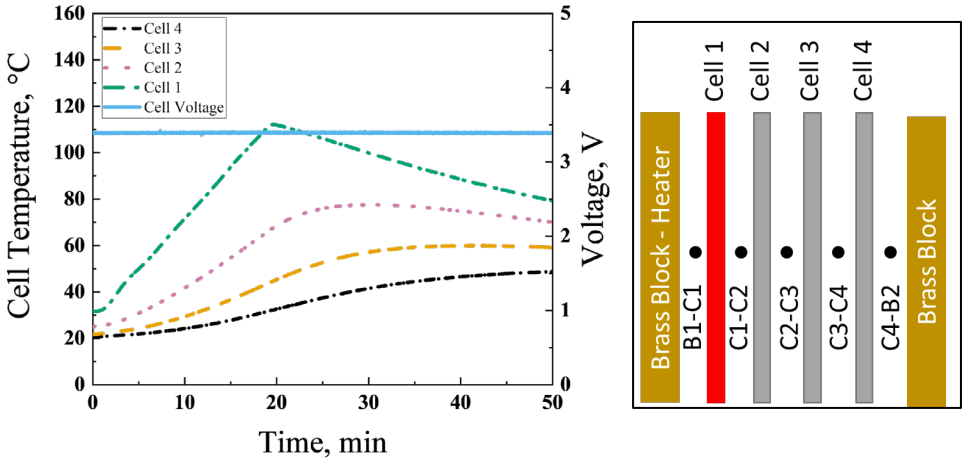

Figure 27. Temperature and voltage response during the OT test of a 1s4p battery pack. The thermocouple mapping (right) illustrates the temperature distribution across the test setup.

Figure 27 shows the voltage and temperature profiles during this intervention experiment. The triggered cell reached a peak temperature of 111° C at the moment the impedance-based failure marker was detected, as shown in Figure 28(a). Immediate deactivation of the heating element led to a gradual decline in temperature, successfully preventing further thermal escalation and averting thermal runaway. This test showed that impedance-based diagnostics can be used for timely intervention in OT conditions to prevent thermal runaway, provided that the failure marker is clearly defined and the system response is rapid.

Notably, the gas sensors remained inactive throughout the test, as shown in Figure 28(b), indicating that cell venting did not occur. This reinforces the idea that gas sensors typically respond later in the failure process, often after irreversible damage has begun, and therefore may be more suitable as confirmation tools rather than early-warning triggers in lower-severity scenarios. Additionally, no changes were observed in the pack voltage during the test, further suggesting that cell degradation had not progressed to a level that disrupted electrochemical function. This is an important outcome, as it suggests that intervention during thermal failures based on impedance monitoring may be executed before any observable signs of failure appear in more conventional diagnostics like voltage or gas evolution.

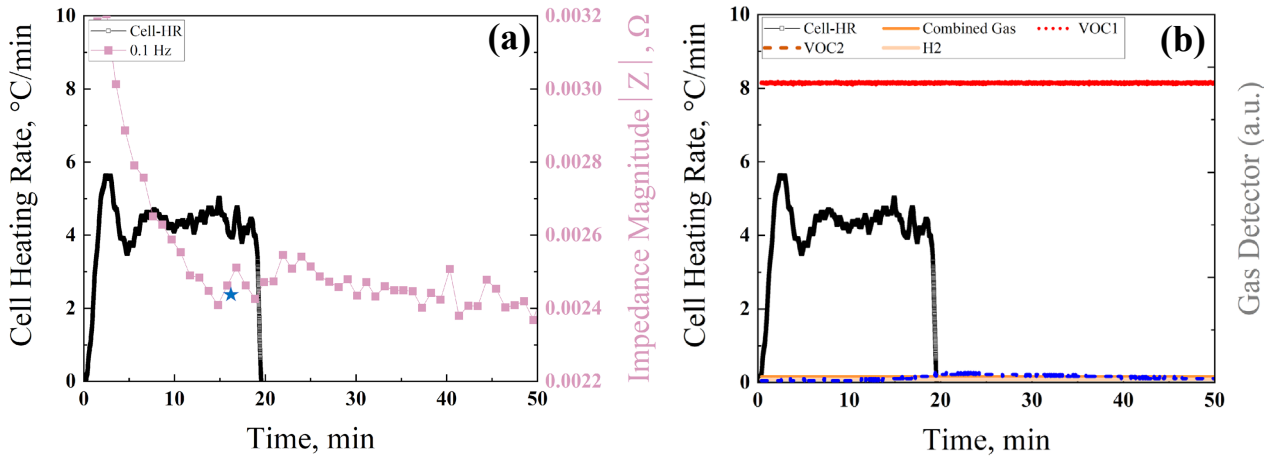

Figure 28. (a) Impedance magnitude at 0.1 Hz, and (b) gas sensor response during OT testing of a 1s4p pack

Conclusions

This study evaluated the performance of rapid EIS and commercially available gas sensors as early warning diagnostics for thermal and electrical abuse in LFP/Gr cells across two or more system configurations, including single cells, parallel-connected packs (1s4p), series-connected packs (4s1p), and parallel-series-connected packs (4p2s). Both OT and OC conditions were assessed using in-operando testing, gas analysis via FTIR and gas sensors, video recording, and time-resolved impedance measurements.

Under OT conditions, rapid EIS provided the earliest $\Delta t_{\text{warning time}}$ across single cells and 1s4p configurations. Electrochemical resistance changes were detectable well before gas release or visible failure, allowing for meaningful lead time in most cases. Gas sensors also performed effectively, particularly VOC2 and the combined-gas sensor, which triggered consistently before major thermal activity. However, warning times were generally shorter than those provided by EIS, as gas evolution tended to occur after initial degradation had already started. These results show that for thermally driven abuse, impedance-based diagnostics may offer early detection capability, even as system complexity increases, provided the signal remains distinguishable from background variation caused by interconnects and pack-level averaging.

During OC events, the results indicated that the changes in electrochemical resistance and gas generation occurred more closely in time, suggesting a more synchronized relationship between these two phenomena. This was especially pronounced in multicell configurations, where venting often occurred before significant impedance change could be detected. As a result, gas sensors outperformed EIS in OC scenarios, particularly in the 1s4p and 4s1p configurations. VOC1, VOC2, and the combined-gas sensor provided earlier warnings relative to EIS. The H_2 sensor was also effective in higher-severity tests. In one instance, however, VOC1 failed to detect venting until well after the failure point, likely due to sensor degradation, calibration drift, or disrupted gas pathways. This result highlights the need to consider long-term stability and placement of gas sensors in real-world systems, where detection performance can be affected by aging, venting direction, or sensor orientation.

Pack architecture significantly influenced diagnostic response. In parallel-connected packs, earlier onsets of failure and greater gas generation were observed, likely driven by current redistribution and thermal interaction between cells. In series-connected packs, the contribution of individual cells to overall impedance became less distinct, leading to shorter warning times and reduced diagnostic resolution. Results indicate that no single diagnostic method provides comprehensive coverage across all failure modes and configurations, as each method has its strengths and limitations. Rapid EIS was most effective during OT events but provided limited warning time during OC, especially in larger packs. Gas sensors offered more consistent performance across tests but were dependent on venting to trigger and therefore may not always provide enough lead time for intervention. Signal delay, sensor placement, and environmental variability all introduce uncertainty that must be considered in practical applications.

Improving diagnostic reliability in future battery systems may require the use of distributed sensing, combining thermal, electrochemical, and gas-based techniques. More localized measurements, improved sensor integration, and real-time signal interpretation could help address the limitations introduced by pack-level signal averaging. Overall, this work highlights the strengths and limitations of different diagnostic strategies under abuse conditions and across varying system scales. The findings support a system-level approach to diagnostics, one that

adapts to the failure mode, battery architecture, and application. Such strategies will be essential to ensure early detection and safe operation as lithium-ion battery systems continue to scale in size and grow in complexity, with increasing cell counts, tighter packing densities, more integrated thermal management, and diverse use cases across electric mobility and stationary energy.

References

Appleberry, M. C., Kowalski, J. A., Africk, S. A., Mitchell, J., Ferree, T. C., Chang, V., Parekh, V., Xu, Z., Ye, Z., Whitacre, J. F., & Murphy, S. D. (2022). Avoiding thermal runaway in lithium-ion batteries using ultrasound detection of early failure mechanisms. *Journal of Power Sources*, *535*, 231423. https://doi.org/10.1016/j.jpowsour.2022.231423

Barkholtz, H. M., Preger, Y., Ivanov, S., Langendorf, J., Torres-Castro, L., Lamb, J., Chalamala, B., & Ferreira, S. R. (2019). Multi-scale thermal stability study of commercial lithium-ion batteries as a function of cathode chemistry and state-of-charge. *Journal of Power Sources*, *435*, 226777. https://doi.org/10.1016/j.jpowsour.2019.226777

Cai, T., Stefanopoulou, A. G., & Siegel, J. B. (2019). Early detection for Li-Ion batteries thermal runaway based on gas sensing. *ECS Transactions*, *89*(1), 85. https://doi.org/10.1149/08901.0085ecst

Cai, T., Valecha, P., Tran, V., Engle, B., Stefanopoulou, A., & Siegel, J. (2021). Detection of Li-Ion battery failure and venting with carbon dioxide sensors. *eTransportation*, *7*, 100100. https://doi.org/10.1016/j.etran.2020.100100

Dong, P., Liu, Z., Wu, P., Li, Z., Wang, Z., & Zhang, J. (2021). Reliable and early warning of lithium-ion battery thermal runaway based on electrochemical impedance spectrum. *Journal of the Electrochemical Society*, *168*(9), 090529. https://doi.org/10.1149/1945-7111/ac239b

Feng, X., Ouyang, M., Liu, X., Lu, L., Xia, Y., & He, X. (2018). Thermal runaway mechanism of lithium-ion battery for electric vehicles: A review. *Energy Storage Materials*, *10*, 246–267. https://doi.org/10.1016/j.ensm.2017.05.013

Finegan, D. P., Scheel, M., Robinson, J. B., Tjaden, B., Hunt, I., Mason, T. J., Millichamp, J., Di Michiel, M., Offer, G. J., Hinds, G., Brett, D. J. L., & Shearing, P. R. (2015). In-operando high-speed tomography of lithium-ion batteries during thermal runaway. *Nature Communications*, *6*(1), 6924. https://doi.org/10.1038/ncomms7924

Gachot, G., Grugeon, S., Eshetu, G. G., Mathiron, D., Ribière, P., Armand, M., & Laruelle, S. (2012). Thermal behaviour of the lithiated-graphite/electrolyte interface through GC/MS analysis. *Electrochimica Acta*, *83*, 402–409. https://doi.org/10.1016/j.electacta.2012.08.016

Golubkov, A. W., Fuchs, D., Wagner, J., Wiltsche, H., Stangl, C., Fauler, G., Voitic, G., Thaler, A., & Hacker, V. (2014). Thermal-runaway experiments on consumer Li-ion batteries with metal-oxide and olivin-type cathodes [10.1039/C3RA45748F]. *RSC Advances*, *4*(7), 3633–3642. https://doi.org/10.1039/C3RA45748F

Hill, D., Gully, B., Agarwal, A., Nourai, A., Thrun, L., Swartz, S., Koslowske, M., Cummings, S., Butkowski, J., & Moore, B. (2013, May 21-23). *Detection of off gassing from Li-ion batteries*. 2013 IEEE Energytech, Cleveland, OH.

Khakani, S. E. L., Rochefort, D., & MacNeil, D. D. (2016). ARC study of LiFePO4 with different morphologies prepared via three synthetic routes. *Journal of the Electrochemical Society*, *163*(7), A1311. https://doi.org/10.1149/2.0801607jes

Klink, J., Grabow, J., Orazov, N., Benger, R., Börger, A., Ahlberg Tidblad, A., Wenzl, H., & Beck, H.-P. (2021). Thermal fault detection by changes in electrical behaviour in lithium-ion cells. *Journal of Power Sources*, *490*, 229572. https://doi.org/10.1016/j.jpowsour.2021.229572

Kvasha, A., Gutiérrez, C., Osa, U., de Meatza, I., Blazquez, J. A., Macicior, H., & Urdampilleta, I. (2018). A comparative study of thermal runaway of commercial lithium ion cells. *Energy*, *159*, 547–557. https://doi.org/10.1016/j.energy.2018.06.173

Lamb, J., Orendorff, C. J., Roth, E. P., & Langendorf, J. (2015). Studies on the thermal breakdown of common Li-ion battery electrolyte components. *Journal of the Electrochemical Society*, *162*(10), A2131. https://doi.org/10.1149/2.0651510jes

Li, Y., Zhao, W., Zhang, G., & Shi, S. (2023, September 12). Unified picture on temperature dependence of lithium dendrite growth via phase-field simulation. *Energy Material Advances*, 4. doi:10.34133/energymatadv.0053

Lyu, N., Jin, Y., Xiong, R., Miao, S., & Gao, J. (2022). Real-time overcharge warning and early thermal runaway prediction of Li-ion battery by online impedance measurement. *IEEE Transactions on Industrial Electronics*, *69*(2), 1929–1936. https://doi.org/10.1109/TIE.2021.3062267

Naylor Marlow, M., Chen, J., & Wu, B. (2024, January 4). Degradation in parallel-connected lithium-ion battery packs under thermal gradients. Communications Engineering, (3)2. doi:10.1038/s44172-023-00153-5. PMCID: PMC10955900

Pasquier, A. D., Disma, F., Bowmer, T., Gozdz, A. S., Amatucci, G., & Tarascon, J. M. (1998). Differential scanning calorimetry study of the reactivity of carbon anodes in plastic Li-ion batteries. *Journal of the Electrochemical Society*, *145*(2), 472. https://doi.org/10.1149/1.1838287

Qiu, M., Liu, J., Cong, B., & Cui, Y. (2023). Research progress in thermal runaway vent gas characteristics of Li-ion battery. *Batteries*, *9*(8), 411. https://doi.org/10.3390/batteries9080411

Shen, H., Wang, H., Li, M., Cheng, L., Zhang, Y., Li, Y., Yang, X., Feng, X., & Ouyang, M. (2023). Thermal runaway characteristics and gas composition analysis of lithium-ion batteries with different LFP and NCM cathode materials under inert atmosphere. *Electronics*, *12*(7), 1603. https://doi.org/10.3390/electronics12071603

Sloop, S. E., Kerr, J. B., & Kinoshita, K. (2003). The role of Li-ion battery electrolyte reactivity in performance decline and self-discharge. *Journal of Power Sources*, *119-121*, 330–337. https://doi.org/10.1016/S0378-7753(03)00149-6

Sun, J., Li, J., Zhou, T., Yang, K., Wei, S., Tang, N., Dang, N., Li, H., Qiu, X., & Chen, L. (2016). Toxicity, a serious concern of thermal runaway from commercial Li-ion battery. *Nano Energy*, *27*, 313–319. https://doi.org/10.1016/j.nanoen.2016.06.031

Torres-Castro, L., Bates, A. M., Johnson, N. B., Quintana, G., & Gray, L. (2024). Early detection of Li-ion battery thermal runaway using commercial diagnostic technologies. *Journal of the Electrochemical Society*, *171*(2), 020520. https://doi.org/10.1149/1945-7111/ad2440

Torres-Castro, L., Kurzawski, A., Hewson, J., & Lamb, J. (2020). Passive mitigation of cascading propagation in multi-cell lithium ion batteries. *Journal of the Electrochemical Society*, *167*(9), 090515. https://doi.org/10.1149/1945-7111/ab84fa

Wu, B., Yufit, V., Marinescu, M., Offer, G., Ricardo, M.-B., & Brandon, N. (2013, December). Coupled thermal-electrochemical modelling of uneven heat generation in lithium-ion battery packs. *Journal of Power Sources,* 243. DOI:10.1016/j.jpowsour.2013.05.164

Yang, H., Bang, H., Amine, K., & Prakash, J. (2004). Investigations of the exothermic reactions of natural graphite anode for Li-ion batteries during thermal runaway. *Journal of the Electrochemical Society*, *152*(1), A73. https://doi.org/10.1149/1.1836126

Yuan, L., Dubaniewicz, T., Zlochower, I., Thomas, R., & Rayyan, N. (2020). Experimental study on thermal runaway and vented gases of lithium-ion cells. *Process Safety and Environmental Protection*, *144*, 186–192. https://doi.org/10.1016/j.psep.2020.07.028

Zhang, M., He, Z., Cheng, W., Li, X., Zan, X., Bao, Y., Gu, H., Homewood, K., Gao, Y., Zhang, S., Wang, Z., Lei, M., & Xia, X. (2024). A room-temperature MEMS hydrogen sensor for lithium-ion battery gas detecting based on Pt-modified Nb doped TiO2 nanosheets. *International Journal of Hydrogen Energy*, *74*, 307–315. https://doi.org/10.1016/j.ijhydene.2024.05.388

DOT HS 813 817
August 2026

U.S. Department
of Transportation

**National Highway
Traffic Safety
Administration**

16979-080526-v3